# Neutron total scattering studies on low cost and high energy density cathode materials in Li-ion batteries

A Thesis Presented for the
Master of Science
Degree
The University of Tennessee, Knoxville

Margarita Petrova
May 2026

Copyright © 2026 by Margarita Petrova.
All rights reserved.

## ACKNOWLEDGEMENTS

I would like to express my deepest gratitude to my major advisor, Prof. Katharine Page, for her invaluable guidance, constant support, and insightful suggestions, as well as for creating an encouraging and supportive learning environment. Her mentorship has had a profound impact on both my academic and personal growth. I am also sincerely grateful to my co-advisor, Dr. Thomas Proffen, for his continuous help, thoughtful feedback, and guidance on my professional development. I deeply appreciate the time and effort of both of my advisors dedicated to sharing their knowledge and experience, as well as their kind support in providing recommendation letters on my behalf.

My research was made possible through the valuable help of Dr. Jue Liu who generously shared his extensive knowledge with me and provided guidance for my growth. I would also like to thank Dr. Peng Zhao for sharing his expertise on Li-ion batteries, which greatly helped me throughout my research. I am further grateful to Dr. Yaocai Bai for his collaboration and guidance in electrochemical measurements related to Li-ion batteries.

I am very thankful to Dr. Bo Jiang for his collaboration on the DRX project and for his significant contributions and support, which enhanced my research experience. I would also like to express my gratitude to Dr. Ethan Self and to Bredesen Center students—Shripad Patel and Max DePrince—for their valuable input on the DRX project and for inspiring discussions that enriched my work.

I am especially thankful to all members of our research group for fostering a strong, supportive environment and their constructive feedback, which helped me improve my research and presentation skills.

I would like to acknowledge the support provided by the Bredesen Center which enabled me to conduct research, participate in professional development activities, and financially support me. I also would like to acknowledge financial support provided by Prof. Page which enabled my research and grew as a professional.

Lastly, I would like to express my heartfelt gratitude to my parents and family for their unwavering love and encouragement during challenging times. Their support has been my greatest source of strength.

## ABSTRACT

The rapid expansion of electric vehicles is driving unprecedented demand for lithium-ion batteries, increasing the need for cathode materials that deliver high energy density while also improving cost, safety, and reliance on earth-abundant elements. This thesis uses neutron total scattering, featuring Bragg diffraction and pair distribution function (PDF) analysis, to connect cathode crystal chemistry, defect formation, and structural evolution across length scales in two representative cathode families: layered nickel–manganese–cobalt oxides (NMC) and manganese-rich cation-disordered rock salt (DRX) oxides.

First, thermal decomposition of highly delithiated NMC is studied using time-of-flight neutron total scattering in an operando gas-flow environment with simultaneous gas analysis. Sequential Rietveld refinement and PDF modeling track the progression from layered order toward a disordered spinel-like structure, with local disorder emerging before complete long-range collapse. Correlating structural metrics with evolved-gas signals provides a direct, bulk-sensitive connection between oxygen release, vacancy formation, and transition-metal migration during thermal abuse.

Second, neutron total scattering is used to quantify average structure, short-range order, and local distortions in Mn/Ti-based DRX Cathodes, emphasizing the need for large-supercell modeling to represent composition-dependent local environments that control Li-transport connectivity.

Overall, this work demonstrates a unified neutron-based framework for understanding and mitigating cathode instability and guiding design of next-generation, earth-abundant materials. The mechanistic connections identified here suggest strategies to improve cathode safety and lifetime by stabilizing the oxygen sublattice, limiting vacancy-enabled transition-metal migration, and engineering short-range order to promote robust Li transport in next-generation, earth-abundant cathode chemistries.

## TABLE OF CONTENTS

CHAPTER ONE: INTRODUCTION ..... 1

CHAPTER TWO: THERMAL DEGRADATION OF NMC 333 ..... 5

CHAPTER THREE: MODELING LOCAL STRUCTURE IN MN-RICH DISORDERED ROCK SALT CATHODES USING PDF ANALYSIS ..... 266

CHAPTER FOUR: CONCLUSIONS AND RECOMMENDATIONS ..... 48

LIST OF REFERENCES ..... 51

VITA ..... 611

## LIST OF TABLES

**Table 1.** Lattice parameters, atomic positions, atomic displacement parameters, and fractional site occupancies resulting from Rietveld refinements for data collected at 234 °C, for layered oxide a=2.8377(3), c=14.329(3) with trigonal lattice, SG R $\bar{3}$m.2)..... 144

**Table 2.** Lattice parameters, atomic positions, atomic displacement parameters, and fractional site occupancies resulting from Rietveld refinements for data collected at 234 °C, for defect spinel a=8. 0.699(5) with cubic lattice, space group Fd-3m (origin position 2).. 144

**Table 3**. Lattice parameters, atomic positions resulting from PDF refinements in range r= 5-15 Å for data set 123872 at temperature 238 °C, for layered oxide (a) a=2.837(3), c=14.198(6) with trigonal lattice, SG R $\bar{3}$m and for defect spinel with Qmax=22..... 166

**Table 4.** Comparison of different models for different structural aspects……28

**Table 5.** List of materials used in this study: one DRX oxide and three oxyfluorides with formula $Li_{1.2}Mn_x\ Ti_{0.8-x}O_{2-y}$, (x=0.4, 0.5, 0.6,0.7 and y=0. 0.1, 0.2, 0.3)..... 32

**Table 6.** List of refined and fixed parameters to refine structures obtained from MC/DFT with PDFgui and test these structures against experimental data ..... 37

## LIST OF FIGURES

**Figure 1.** Structural components in a Li-ion battery [10]. Credits: (Diagram by Argonne National Laboratory, licensed under CC BY-NC-SA 2.0) ..... 3

**Figure 2.** Experimental setup for study of thermal decomposition of NMC333 with neutron total scattering and operando gas analysis. ..... 133

**Figure 3.** Select Rietveld refinement fits to experimental NMC333 neutron diffraction data using the initial layered structure collected at (a) 100.4 °C (Rwp= 2.859), (b) 234 °C (Rwp= 3.478), and (c) 539 °C (Rwp= 4.502). Data are given as black lines, fits as red lines, and difference curves fall below the data and fits as blue lines.... 166

**Figure 4**. PDF fits for different temperatures with layered model in r range 5-15 Å. Selective fits to neutron total scattering data after PDF refinements for 87 °C (Rwp= 16.8), for 119 °C (Rwp= 14.98), and for 184 °C (Rwp= 15.87)..... 188

**Figure 5. (a)** Three models used to fit neutron scattering data collected from in operando thermal decomposition experiment. **(b)** Waterfall plot showing diffraction patterns collected from room temperature up to 550 °C. **(c)** Oxygen partial pressure and temperature as a function of time. The evolution of oxygen gas is closely related to phase transitions that occur during thermal decomposition……19

**Figure 6. (a)** Layered oxide structure (SG $R\bar{3}m$) with key characteristics labelled. 3a sites are occupied by Li and Ni. During thermal decomposition some Li ions migrate to the transition metal layer (3b sites) occupied by Co, Ni and Mn, creating increased structural disorder. **(b)** Lattice parameters a and c, and **(c)** Ni occupancy in NMC 333 from Rietveld analysis as a function of temperature. Sequential refinements

were performed using the layered structure model (SG R$\bar{3}$m), which has lower symmetry compared to the disordered spinel phase (SG Fd$\bar{3}$m). ..... 200

**Figure 7. (a)** Layered structure model used to fit PDF data over the entire range of the in operando thermal decomposition experiment. **(b)** Waterfall plot showing PDF patterns, G(r), collected from room temperature up to 550 °C. **(c)** Oxygen partial pressure and temperature as a function of time. ..... 211

**Figure 8 (a)** z coordinate for oxygen **(b)** ratio of lattice parameters c/a and cell volume PDF refinements were performed in range r= 10-20 Å. ..... 222

**Figure 9. (a)** Unit cell volume and **(b)** c/a ratio parameters resulting from Rietveld and PDF refinements (r=5-15 Å range) of NMC333 data collected during in situ thermal degradation. The temperature ranges corresponding to observed oxygen evolution peaks during thermal degradation are shown as solid rectangles (1$^{st}$ peak between 300 and 354 °C in green; 2nd peak between 378 and 424 °C in blue; and 3rd peak between 454 and 548 °C in pink)..... 244

**Figure 10.** Comparison of specific energy and specific capacity of different cathode materials with those of DRXs, [76] ..... 277

**Figure 11. (a)** Crystal structure of a cation disordered rock salt type (lithium metal oxide) and **(b)** Schematic energy landscape for migration of lithium from its octahedral site through a tetrahedral vacancy to another octahedral site [82]. ..... 300

**Figure 12**. Calculated total and partial PDFs for disordered model in four compositions in r-range 1.5-6 Å..... ..35

**Figure 13.** Schematic for small and big box modelling ..... 37

**Figure 14.** Rw resulting from PDF refinement of Mn0.5 data using 100 different structure models relaxed with a DFT GGA functional – MC-DFT(GGA)..... 38

**Figure 15.** Comparison of PDF fits using different models for Mn0.4 data. The left column of figures shows PDF refinements in the range of 1.5-12 Å, while the right column of figures shows refinement in the range of 1.5-25 Å ..... ..40

**Figure 16.** Goodness of fits results for range dependent PDF refinements of data from four DRX compositions using 5 models..... 43

**Figure 17.** Correlation length as the function of Mn content from analysis with car box PDF refinements up to 34 Å for 5 different models ..... 44

**Figure 18.** Violin plots showing distribution of bond length for (a) Ti-O, (b) Mn-O, and (c) Li-O for composition Mn0.4 with refined PDF using the MC-GGA model. PDF refinements were done in r-range 1.5-12 Å for five best structures which have the lowest Rw values. These 5 structures were selected from 100 refined structures. Each violin corresponds to a certain material composition……...45

# CHAPTER ONE: INTRODUCTION

## 1.1 Background and Statement of the Problem

Growing adoption of electrical vehicles (EV) is causing an increase in the demand of Li-ion batteries (LIBs) in the market. It is estimated that the global demand of energy from LIB will be around 50 TWh in 2040, with the electric mobility sector accounting for 30 TWh [1].

To meet requirements for growing demand, LIBs must store enough energy per weight for a vehicle to travel long distance. This significant factor, the energy density, is a critical factor determining how many miles a charged vehicle can travel. The highest specific energy density in a modern Li-ion battery is 220 Wh/kg [2]. Life span is another important parameter in LIB. The life span of EV batteries is measured in cycles. One cycle represents full charge and discharge. A typical EV battery performs 1000-2000 charge/discharge cycles [3]

The major components of a LIB are shown in Figure 1. A key technology bottleneck of the Li-ion battery is the cathode. Cathode materials are designed for extracting and re-inserting Li-ions via the electrolyte, and this process is called intercalation and deintercalation. This thesis applies neutron diffraction and neutron pair distribution function techniques to explore key characteristics of two types of high energy density solid state cathodes: (1) layered nickel–manganese–cobalt oxides (NMC) and (2) manganese-rich cation-disordered rock salt (DRX) oxides.

NMC is one of the most common types of LIB used in contemporary EVs. NMC is made from Lithium-Nickel-Manganese-Cobalt-Oxide, featuring a basic chemical formula of $(Li/Ni/Mn/Co)O_2$. The main advantage of NMC batteries over the prevalent lithium- iron phosphate (LFP) batteries is higher energy density [4].

One of the main disadvantages of NMC is high cost, driven by recent increases in the cost of nickel and cobalt for cathode production. For example, NMC battery cost increased by 15% in 2022 alone [5], driven by mineral supply constraints. For example, about 60 % of global mining for Co is undertaken in a single country, the Democratic Republic of Congo [6]. This has led to a shift toward lower cobalt chemistries and increased demand for nickel. Though nickel sources for mining are more geographically

diverse compared to cobalt, the available supply currently lags demand. Cobalt and nickel are included in the list of 50 mineral commodities critical to the U.S. economy and national security, according to the U.S. Geological Survey in 2022 [7]. Therefore, there is great need for transitioning to more extensive use of earth abundant-based cathodes (chemistries including Mn, Fe, Ti, etc.) which will contribute to a reduction of USA dependence on critical minerals. NMC chemistries (with inclusion of Mn) intentionally feature decreased Ni and Co content.

A major disadvantage of NMC cathodes is their poor thermal stability due to Ni migration into Li sites and formation of oxygen vacancies disrupting Li-ion pathways, increasing resistance and accelerating capacity fade during cycling or thermal exposure. Multi-step oxygen release during degradation additionally poses safety risks, as reactive oxygen can trigger parasitic reactions, electrolyte decomposition, and thermal runaway, particularly in the presence of organic electrolytes [8]. The mechanisms of these technology limitations require more study.

More extensive chemical substitution to achieve earth abundant-based cathodes with improved material properties and lower cost has led to investigation of disordered rock salt (DRX) cathodes, a relatively new class of cathode materials for LIB. These cathodes feature high concentrations of more abundant and less expensive metals such as manganese and titanium. Disorder present in this material structure is key to enhanced electrochemical properties, and must be further studied to understand and improve Li-ion insertion and removal during charging and discharging cycles [9].

In particular, DRX cathodes suffer from poor cycling stability. Since DRX materials rely on oxygen redox reactions for their capacity, often oxygen redox reactions lead to irreversible oxygen loss which causes changes in structure and material degradation in repeated charge/discharge cycles [9]. In addition, some DRX materials heavily rely on nickel redox which can cause gas evolution of $CO_2$ and $O_2$ during cycling. As a result, this gas evolution causes densification of material surfaces which leads to poor ion transport and capacity fade [11].

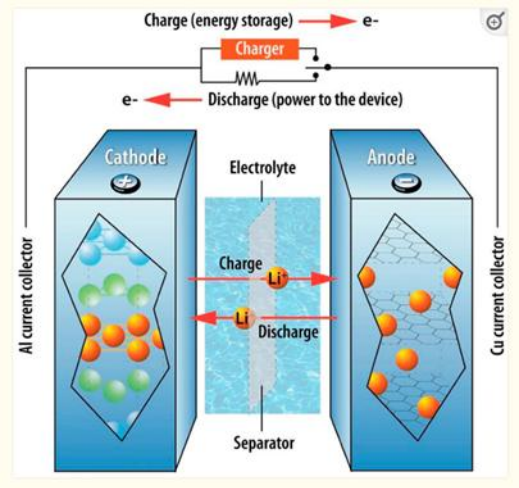


**Figure 1.** Structural components in a Li-ion battery [10]. Credits: (Diagram by Argonne National Laboratory, licensed under CC BY-NC-SA 2.0)

Overall, advanced cathode materials with higher energy density and lower cost determine the future of Li-ion batteries to meet the increasing demand for electrical vehicles [12]. It is important to implement crystal-chemical design strategies to develop low cost and high energy density materials with improved safety. An additional benefit of these strategies is a reduction of USA dependance on critical minerals needed for production of high energy density battery materials.

### 1.2. Neutrons as a Critical Tool to Investigate Technology Bottlenecks

Neutron total scattering is a diffraction technique in which both Bragg and diffuse scattering intensities are measured over a wide range of momentum transfer. This provides a means for average and local structure features to be analyzed together. Neutron scattering methods exhibit high sensitivity for light elements, including lithium and oxygen, which allows the positions and occupancies of these elements (as well as their vacancies or interstitials) to be determined [13].

Neutron Pair Distribution Function (PDF) analysis probes local atomic environments and allows one to detect deviations from long-range order, including stacking faults and intergrowths in battery materials [14]. Additionally, the ordering/disordering of cations in metal layers of cathode materials can be determined with

the technique [15]. These and other departures from ideal order (defects) can provide significant contributions to the electrochemical performance of batteries.

In-situ or operando neutron total scattering experiments enable the probing of structural changes and exploration of defect evolution during electrochemical cycling of battery materials in real-time. This capability allows one to shed light to mechanisms of defect formation under operating conditions [16]. In addition, neutrons have high penetration depth compared to X-rays, making them suitable for probing large cell sizes including commercial Li-ion cells. Consequently, neutron total scattering is one of the most powerful techniques to study defect chemistry and understand functional properties in battery materials.

This thesis will examine how neutron total scattering methods can be applied to study critical technology gaps in high energy density cathode materials. Chapter 2 addresses the thermal stability of the layered oxide cathode material $Li_{0.3}Ni_{1/3}Mn_{1/3}Co_{1/3}O_2$ (NMC333). This material was investigated using total neutron scattering and operando gas analysis during heating up to 550 °C to address safety-critical processes that occur during Li-ion battery thermal runaway. By simultaneously probing the average and local structure and monitoring $O_2$ evolution, the mechanisms governing thermal decomposition in the highly delithiated cathode were examined. Chapter 3 investigates the average structure and short-range order in four Mn- and Ti-rich DRX materials with neutron total scattering. A variety of theory and modeling techniques are used to model short range order (SRO) structures and fit experimental neutron PDF data. Perspectives and future directions are offered in Chapter 4.

# CHAPTER TWO: THERMAL DEGRADATION OF NMC 333

## 2.1 Introduction

The rapid global expansion of electric vehicles (EVs), driven by rising consumer demand and aggressive industry investment, has intensified the need for safer and more durable battery technologies. One of the most commercialized LIB cathode material classes s the mixed metal oxide containing nickel, manganese, and cobalt, categorized as 'NMC' for short. The general formula for these oxides is $LiNi_xMn_yCo_{(1-x-y)}O_2$. Batteries with this type of cathode have high energy density which enables EVs to drive longer distances. Different ratios of Ni, Mn, and Co allow one to optimize performance according to specific requirements for vehicles. For example, newer compositions such as NMC811 consisting of 80% Ni, 10% Mn, and 10% Co, have a reduced Co content and maintain high energy density[17]

Varying amounts of metals and doping with different elemental changes can induce changes in crystal structure and local oxygen environments which control oxygen release, phase transition, and the amount of heat generated during thermal abuse. It is important to have thermally stable materials during LIB operation to avoid the risk of thermal runaway and fires. We will examine recent research on the crystal chemistry of NMC cathodes involving neutron scattering and present our own work on thermal degradation of this material type with operando neutron scattering methods.

### 2.1.1 Effect of Ni/Mn content on NMC structure

The effect of increasing Ni content on NMC structure was investigated using neutron powder diffraction (NPD) methods for three materials: NMC 433, NMC 622, and NMC 811 in work by Thomas E. Ashton et al. [18]. They used a model of $(Li_{1-d}Ni_d)_{3b}(Li_gNi_{x-g}Mn_yCo_z)_{3a}O_2$ with $R\bar{3}m$ structure in Rietveld refinements to establish mixing of $Li^+$ and $Ni^{2+}$ in 3a and 3b lattice sites. Their investigation showed that materials NMC 811 and NMC 622 have a R $\bar{3}$m structure like the $LiMO_2$ (M=Ni, Mn, Co) phases. Lowering Ni concentration led to dramatic change in structure with the formation of three phases in NMC 433. The work suggested this change was caused by the presence of an increased amount of Mn. This conclusion aligns with findings of increased cation mixing in the experimental work by L. Yin et al. [19], induced when Ni is replaced by Mn. The

changing cation content modifies Ni-O bond lengths and Ni coordination, affecting the local atomic environment.

### 2.1.2 Iron (Fe) doping and substitution

The crystal structure of NMC becomes unstable during prolonged cycling and causes materials degradation. In work by Juliette Billaud et al [20], the effects of Fe doping and substitution were investigated on electrochemical performance in two groups of materials cycled at high rates. In the first group (Fe substitution), the amount of Li was held identical to the reference material with nominal composition of $Li_{1.17}(Ni_{0.23}Co_{0.12}Mn_{0.65})_{0.83}O_2$, but with added Fe, referred to as $Li_{100}Fe_x$ NCM material. In the second group (Fe doping), Li was partially replaced with Fe during the synthesis stage with the molar ratio 3:1, referred to as $Li_{100-3x}$ $Fe_x$ NCM material. Phases present in the material and phase fractions were investigated with the use of neutron powder diffraction.

This investigation showed the presence of the monoclinic $Li_2MnO_3$ phase (*C*2/*m* space group) structure in all compositions except the reference material. Fe doping in the second group led to the formation of an additional spinel phase ($LiM_2O_4$, space group *Fd*3*m*).

Electrochemical measurements demonstrated increased specific charge, enhanced capacity retention, and stable potential during cycling at high rates, especially for $Li_{1.16}(Ni_{0.18}Co_{0.10}Mn_{0.52}Fe_{0.02})O_2$. This compound was reported to hold specific charge up to 150 mAh $g^{-1}$at 4C rate and capacity retention of 93% after 100 cycles, suggesting an increased Li capacity. The increased specific charge and more stable cycling behavior of the material was linked to the electrochemical activity of Fe in the structure, which was confirmed by X-ray photoelectron spectroscopy. This work stressed the importance of either doping or substituting small amounts of elements in materials to improve their electrochemical performance.

### 2.1.3 Fluorine (F) doping and substitution

Recently, work by Hong Cai et al. [21] has been completed on oxyfluoride $Li_{1.25}Ni_{0.625}Mn_{1.125}O_3F$ with partial spinel like cation vacancy ordering. The crystal structure was determined with Rietveld refinement using XRD and neutron diffraction data

as a cubic structure, *Fd*-3*m*. This material showed high capacities of 225 and 285 mAh $g^{-1}$ for temperatures of 25 and 40 °C, respectively. This additional capacity can be explained by Mn redox at low potentials and Li intercalation in the lattice. Raman analysis and ex situ XRD of cycled samples at different states of charge /discharge confirmed a single phase de(lithiation) reaction mechanism over a large range of potential. Doping material with F presents an opportunity to control site occupancy and oxidation states by changing the charge states of anions in sublattice. It allows further incorporation of lower charge $Ni^{+2}$ cations into the process, enhancing material performance.

**2.1.4 Chromium (Cr) doping and substitution**

High energy nickel-cobalt-manganese oxides (HE-NCM) were studied by Thackeray et al. [22]. HE-NCM have a general formula $Li_{1+x}Ni_aCo_bMn_cO_2$ and high specific capacity up to 260 mAh/g. Literature describes the structure of HE-NCM featuring macroscopic areas composed with two distinct phases: rhombohedral $LiMO_2$ (space group R $\bar{3}$m) The work by Sébastien Sallard et al, [23] studied the effect of Cr doping/substitution in HE-NCM on potential drop during cycling. The ratio between different transition metals (TM) was kept constant. They used two strategies in their studies: 1) substitution of 1 $Cr^{3+}$ replacing 3 $Li^+$, denoted Li/Cr; and 2) Cr-addition, referred to as doping. For doping, the amount of Li was kept the same as in the reference material, HE-NCM. Using neutron diffraction measurement, they found that Cr addition leads to minor changes in crystal structure and affects the $Li_2MnO_3$ phase. Inter-site ion exchange for Ni and Li was observed in this phase. An increase in average discharge potential of 50 mV was reported for compositions with high Li/Cr ratios. For Cr substitution, the material with the composition of $Li_{95}Cr_{1.67}$-NCM demonstrated a mitigation in potential drop during cycling. In $Li_{100}Cr_{3.33}$-NCM compound, the potential shift was reduced by 2/3 after 40 cycles.

Overall, recent literature shows that both cation and anion substitution and doping modify local bonding and changes covalency in NMC cathodes, affecting the crystal structure and cation migration tendencies. Changing the Ni content reshapes the local oxygen coordination and Ni redox, which are important markers of oxygen release and phase transition at higher temperature. Thus, key structural descriptors in the thermal

degradation of layered cathodes include the local Ni-O environment and the extent of Ni/Li mixing.

### 2.1.5. Release of oxygen and other phenomena during thermal decomposition

Despite their advantages, NMC cathodes present safety challenges due to complex electrochemistry. Overcharging or thermal abuse can trigger thermal runaway, a self-accelerating chain reaction where exothermic reactions release heat, potentially causing fire or explosion. Key steps during thermal decomposition on these cathode materials include: (1) decomposition of the solid electrolyte interphase (SEI) at ~80 °C [24]; (2) electrolyte decomposition at 100–200 °C, releasing flammable gases [25]; and (3) cathode breakdown at ≥150 °C, releasing oxygen that reacts with the electrolyte or anode. Limited heat dissipation accelerates these reactions, making external cooling ineffective [26].

Ni-containing layered cathodes, such as $LiNi_{0.33}Mn_{0.33}Co_{0.33}O_2$ (NMC 333) crystallize in a layered *R*-3*m* structure with alternating Li and transition metal (TM) layers. Elevated temperatures enhance Li mobility, prompting Li migration into TM sites. This reduces Li-site occupancy, weakens electrostatic screening, increases O–O repulsion, and expands interlayer spacing, destabilizing the layered framework [27]. Oxygen can be released according to

$$O^{2-} \rightarrow 1/2O_2(g) + 2e \quad \text{(Eq. 1)}$$

with electrons reducing TM ions, primarily $Ni^{4+} \rightarrow Ni^{3+} \rightarrow Ni^{2+}$ [28]. Ni reduction weakens Ni–O bonds, further destabilizing the structure and promoting oxygen evolution, phase transitions, and microcracking. Thermal degradation is governed by TM migration, Li diffusion, oxygen redox activity, and structural changes [29].

Experimental and computational studies have investigated these phenomena. DFT combined with XRD shows oxygen evolution in delithiated $LiNiO_2$ is thermodynamically favorable but kinetically hindered in bulk (~2.4 eV migration barrier), whereas surface migration is facilitated by greater free volume [30]. Techniques such as XRD [31], [32], [33], thermogravimetric analysis (TGA), differential scanning calorimetry (DSC) [34], [35], [36], and accelerating rate calorimetry (ARC) [37], [38] have been widely used.

Studies of $LiNi_{1.02}O_2$ and $LiNi_{0.89}Al_{0.16}O_2$ have examined oxygen release alongside structural changes [39], whereas TR-XRD combined with mass spectrometry (MS) directly correlated structural transformations with oxygen evolution in $LiNi_xCo_{0.15}Al_{0.05}O_2$ [40]. Higher Ni content generally lowers the onset temperature of phase transitions and intensifies oxygen release [41].

Layered LNMO cathodes illustrate the impact of cation ordering on thermal stability. Disordered LNMO forms intermediate phases en route to $NiMn_2O_4$ spinel, releasing oxygen at lower temperatures, whereas ordered LNMO bypasses intermediates and evolves oxygen at higher temperatures, demonstrating superior stability [42]. Recent reviews highlight that oxygen loss induces TM reduction, vacancies, phase transitions, and microcracking, but correlating oxygen evolution with local structural changes remains challenging [43], [44], [45].

A study of spinel $LiNi_{0.5}Mn_{1.5}O_4$ material at elevated temperature was done in several works [46], [47]. It is reported that spinel material exhibits fast decrease in capacity at elevated temperature. A thermodynamically unstable phase can be formed if a high amount of Li is removed from the cathode. This unstable phase decomposes very easily with the release of gaseous $O_2$, and a phase transition takes place. This transformation can lead to thermal explosion [48].

Structural evolution as temperature increases from 25 to 600 °C in commercially available NCM cathodes was reported in work by K.-W. Nam et al. [49]. They observed a phase transition from layered rhombohedral (R $\bar{3}$m) phase to spinel (Fd $\bar{3}$m ), and then to rock salt phase (Fm $\bar{3}$m). This process was accompanied by migration of transition metal ions and release of $O_2$. The increase in the amount of Ni from 40 at % in MNC 433 to 80 at % in NCM811 changed the temperature of phase transition onset, [50**],** [51]. This research work shows how Ni content in the local coordination shell makes oxygen less stable during thermal abuse.

In work by Sung-Kyun Jung et al. [52,], the role of transition metal ions in phase transitions during thermal degradation was studied for Ni-Co-Mn cathodes ($Li_xNi_{0.5}Co_{0.2}Mn_{0.3}O_2$ (x = 1, 0.8, 0.6, 0.5, 0.33) using in situ neutron diffraction and gas analysis from room temperature to 600 °C at intervals of 40-50 °C with a heating rate of

10 °C/minute. The experimental data show that the formation of $Co_3O_4$ type spinel is accomplished mainly by Co cation migration at 430 °C for both compositions. This migration takes place from octahedral sites in TM layers to tetrahedral sites in Li layers. During this transition, reduction from $Co^{3+}$ to $Co^{2+}$ is accompanied by $O_2$ release. It is suggested that Co plays an important role in mitigating oxygen evolution and rock salt phase formation. Tuning this reduction can be used to delay the transition to rock salt phase in the design of NMC cathodes with high safety.

Conventional local probes have substantially advanced our understanding of thermal decomposition in layered oxides, but important gaps remain. Operando X-ray absorption spectroscopy (XAS/XAFS) at multiple edges has been used to follow transition-metal redox and short-range coordination changes during heating and electrochemical perturbation, yet its element-specific, ensemble-averaged signal and sensitivity limits make it difficult to detect small-volume secondary phases or dilute oxygen-release products without extensive multi-edge experiments and careful modelling [53]. Solid-state NMR — most notably recent 17O Nuclear Magnetic Resonance (NMR) spectroscopy studies — can directly probe oxygen environments and Li dynamics, but they require isotope enrichment, suffer from severe paramagnetic broadening in Ni/Mn/Co-rich oxides, and remain experimentally demanding for in-situ/high-temperature measurements [54]. Mössbauer spectroscopy provides local electronic/valence information but is essentially restricted to Fe-containing systems and therefore cannot be broadly applied to Ni-rich layered cathodes [55]. Together, these constraints — detection limits, isotope or isotope-specificity requirements, and beam- or temperature-environment challenges, — limit how fully single local probes can map the onset and spatial heterogeneity of oxygen loss and cation rearrangement during thermal decomposition. By combining neutron total scattering (sensitive to both average and local structure and to light elements such as oxygen) with operando gas analysis (direct, quantitative detection of evolved $O_2/CO_2$) one can directly correlate evolving short-range structure with the timing and quantity of 3 gaseous products, providing the complementary, bulk-sensitive link that many XAS/NMR/Mössbauer studies cannot unambiguously establish.

In order to probe local atomic structure, Pair Distribution Function (PDF) analysis has emerged as a powerful tool. This analysis includes short-range cation ordering, stacking faults, and intergrowths critically impacting battery performance and degradation [56]. For example, PDF studies on $LiNi_{0.5}Mn_{1.5}O_4$ indicate that Ni/Mn ordering domain size affects electrochemical performance more than the degree of Ni/Mn mixing, highlighting the importance of nanoscale structural characterization [57].

For this work, NMC 333 was selected due to its moderate energy density (150–180 Wh/kg) [58] and combination of good thermal stability and long cycle life [59], though it remains prone to oxygen release, microcracking, and cation mixing during cycling [60], [61]. We have integrated neutron total scattering with operando gas-flow measurements, establishing a comprehensive framework to connect long- and short-range structural evolution with oxygen release in cathode materials. Neutrons offer enhanced sensitivity to light elements such as Li and O, allowing accurate determination of site occupancies, defects, and migration pathways [62]. Their high penetration depth ensures bulk-sensitive measurements, while strong elemental contrast from coherent scattering lengths (negative for Li and Mn; positive for Ni, Co, O) enables detection of subtle cation rearrangements [63]. Fourier transformation of total scattering data yields PDF, providing real-space insight into local coordination, stacking faults, and disorder invisible to conventional XRD [14]. This approach provides mechanistic insight into thermal instability in layered oxide cathodes, addressing a critical gap in correlating local atomic structure with reactive oxygen evolution.

## 2.2 Experimental and Computational Details

### 2.2.1 Materials synthesis

The NMC 333 cathode material was synthesized via a conventional solid-state reaction following the procedure of Saaid et al. [64]. NMC 333/graphite pouch cells were fabricated at the Battery Manufacturing R&D Facility, Oak Ridge National Laboratory (ORNL). Composite electrodes were fabricated by mixing NMC 333 with polyvinylidene fluoride (PVDF) binder and conductive carbon black in N-methyl-2-pyrrolidone (NMP) solvent, followed by casting onto aluminum foil and drying at 120 °C under vacuum. The anode consisted of graphite mixed with PVDF binder, cast onto copper foil. Both electrodes

were calendared to achieve uniform thickness and density, then punched into discs for electrochemical cells.

To obtain partially delithiated NMC 333, electrochemical delithiation was performed under a constant-current charge at a C/10 rate, targeting ~70-75% lithium content. Upon reaching the desired state of charge (SOC), the pouch cells were disassembled in an argon-filled glove box. Cathodes were carefully recovered, rinsed with dimethyl carbonate (DMC) to remove residual electrolyte and dried under vacuum. Active material was gently scraped from the aluminum current collector to minimize contamination and was used as powder for neutron scattering experiments.

### 2.2.2 Neutron Total Scattering for In Situ Thermal Degradation

Neutron diffraction and pair distribution function (PDF) measurements were conducted at the Nanoscale Ordered Materials Diffractometer (NOMAD) beamline, Spallation Neutron Source (SNS), ORNL [65]. Approximately 2 g of recovered NMC 333 powder was loaded into a quartz tube (inner diameter 5 mm, wall thickness 0.1 mm) and held in place with quartz wool plugs. Operando oxygen evolution was monitored using a custom high-precision gas flow cell shown in Figure 3. One end of the tube was connected to argon carrier gas, while the other was coupled to a residual gas analyzer (RGA. Exhaust gases, including Ar, $O_2$, $CO_2$ were tracked as a function of time, integrated with encoded sample conditions [66].

One end of the tube was connected to argon carrier gas, while the other was coupled to a gas analyzer. Diffraction data were continuously collected as the sample was heated from room temperature to 550 °C slightly over 11 hours and separated into 102 data sets. The temperature limit of 550 °C was selected to fully capture the irreversible thermal degradation of the highly delithiated layered NMC oxide (≈25% Li). At this level of delithiation, the layered structure is strongly destabilized, and oxygen release, transition-metal reduction, and collapse of the R-3m framework into disordered spinel/rock salt-like phases are known to become pronounced above ~400–500 °C [67]. Holding the sample at 550 °C ensured completion of these degradation processes, enabling robust correlation between oxygen evolution measured operando gas analysis and both long-range and local structural changes probed by neutron total scattering. A few additional holds in temperature

profile were completed, enabling, for example, data collection for one hour at 350 °C. Around this temperature, transition-metal migration is taking place so there is coexistence of two phases. Overall, this setup enabled real-time observation of temperature-dependent structural responses, phase transformations, and oxygen release.

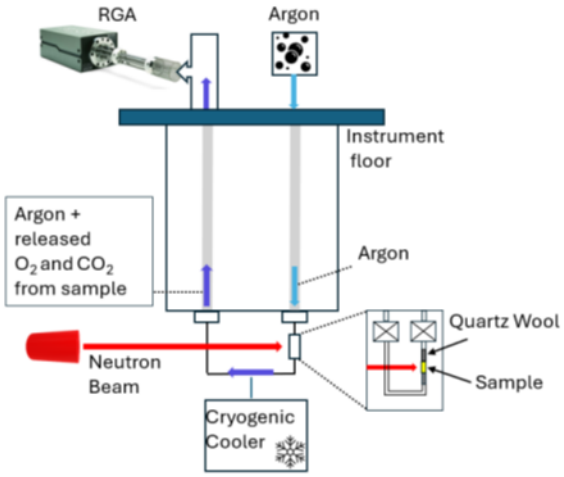


**Figure 2.** Experimental setup for study of thermal decomposition of NMC333 with neutron total scattering and operando gas analysis.

Neutron events were first recorded as time-of-flight (TOF) data with precise detector positioning. TOF data were binned into histograms and mapped to the scattering vector $Q$, based on instrument geometry. For PDF analysis, data were binned in $Q$-space and merged from six detector banks, each with distinct scattering angles. The merged total scattering structure function, $S(Q)$, was Fourier transformed to obtain the pair distribution function, $G(r)$, using a $Q_{max} = 22$ Å$^{-1}$. Standard background subtraction, normalization, and error propagation were applied using the ADDIE software suite [68].

### 2.2.3 Data Modeling

Sequential Rietveld refinements were performed over ~120 temperature points using the TOPAS software suite (version 6) [69]. TOF data were converted to $d$-spacing via a second-order polynomial:

$$TOF = ZERO + DIFC \cdot d + DIFA \cdot d2 \quad \text{(Eq. 2)}$$

where ZERO is an offset, DIFC is the diffractometer constant, and DIFA accounts for sample displacement [70]. NIST certified standard reference material (NIST Si 640e) [71] was used to calibrate ZERO and DIFC, while DIFA was refined. Empirical absorption corrections for Li and Co were applied using the Lobanov function [72]. Peak profiles were modeled using back-to-back exponentials for low-resolution banks and moderator-induced asymmetric functions for high-resolution banks, convoluted with pseudo-Voigt functions for optimal representation.

Refinements started from a trigonal R$\bar{3}$m layered oxide model, refining scale factor, zero shift, background, unit cell parameters, peak profile parameters, oxygen positions, isotropic atomic displacement parameters (ADPs), and cation occupancies in TM and Li layers. Structural metrics, including Li–O and Ni–O bond lengths, were extracted from Rietveld results. Representative Rietveld fits from selective temperatures are shown in Figure 4. Example model parameters used during Rietveld refinements (234 °C data) are given in Table 1 and Table 2.

**Table 1.** Lattice parameters, atomic positions, atomic displacement parameters, and fractional site occupancies resulting from Rietveld refinements for data collected at 234 °C, for layered oxide a=2.8377(3), c=14.329(3) with trigonal lattice, SG R $\bar{3}$m.2).

| **Atom** | **Wyck.** | **x** | **y** | **z** | **Beq (Å$^2$)** | **Frac.** |
|---|---|---|---|---|---|---|
| Li | 3a | 0 | 0 | 0 | 3.48(1) | 0.25 |
| Ni | 3a | 0 | 0 | 0 | 0.7(4) | 0.20 (4) |
| Co | 3b | 0 | 0 | 0.5 | 0.7(4) | 0.3333 |
| Ni | 3b | 0 | 0 | 0.5 | 0.7(4) | 0.11(2) |
| Mn | 3b | 0 | 0 | 0.5 | 0.7(4) | 0.3333 |
| O | 6c | 0 | 0 | 0.2630(2) | 1.2(1) | 0.8(1) |

**Table 2.** Lattice parameters, atomic positions, atomic displacement parameters, and fractional site occupancies resulting from Rietveld refinements for data collected at 234 °C, for defect spinel a=8. 0.699(5) with cubic lattice, space group Fd-3m (origin position 2).

| Atom | Wyck. | x | y | z | Beq (Å$^2$) | Frac. |
|---|---|---|---|---|---|---|
| Li | 8a | 0.125 | 0.125 | 0.125 | 3 | 0.13(4) |
| Ni | 16d | 0.5 | 0.5 | 0.5 | 0.5 | 0.00(2) |
| O | 32e | 0.2331(8) | 0.2331(8) | 0.2331(8) | 1.5 | 1 |
| Ni | 16 | 0 | 0 | 0 | 0.5 | 0.06(2) |

Beq is a scaled representation of isotropic displacement parameter, Uiso. This parameter reflects thermal vibration of atom and static disorder (atom off centering from ideal atomic position). The parameter Beq has the following relationship with Uiso:

$$Beq = 8\pi^2 Uiso \quad \text{(Eq. 3)}$$

It has units of Å$^2$. Typical Ni values for Beq (Ni) are 0.25-0.8 Å$^2$, with larger values indicating significant local disorder. The large Beq for lithium and oxygen in Tables 1 and 2 reflect large local distortion of the Li and oxygen sublattices.

PDF analysis was performed in real-space for $r$ = 5–15 Å using "small-box" modeling in TOPAS, starting from Rietveld-derived structures. Low-r modeling (0.9–4.9 Å) is avoided due to the presence of pair correlations from amorphous carbon contamination in the recovered powder. Refined parameters included unit cell dimensions, oxygen positions, isotropic ADPs for Li, TM (Ni, Mn, and Co, all constrained to be equivalent), and O atoms, and Ni occupancies in both TM and Li layers. The $\delta_1$ parameter, accounting for $r$-dependent peak sharpening due to correlated motion, was also refined. Representative PDF fits from selective temperatures are shown in Figure 5. Example model parameters used during PDF refinements (234 °C data) are given in Table 2.

Rietveld and PDF fits were evaluated using the weighted residual, $R$w:

$$R_w = \sqrt{\frac{\Sigma_i w(r_i)[G_{\text{obs}}(r_i) - G_{\text{calc}}(r_i)]^2}{\Sigma_i w(r_i) G_{\text{obs}}^2(r_i)}} \quad \text{(Eq.4)}$$

where $w(r_i)$ is the inverse square of uncertainty in $G_{\text{obs}}(r_i)$ [73]

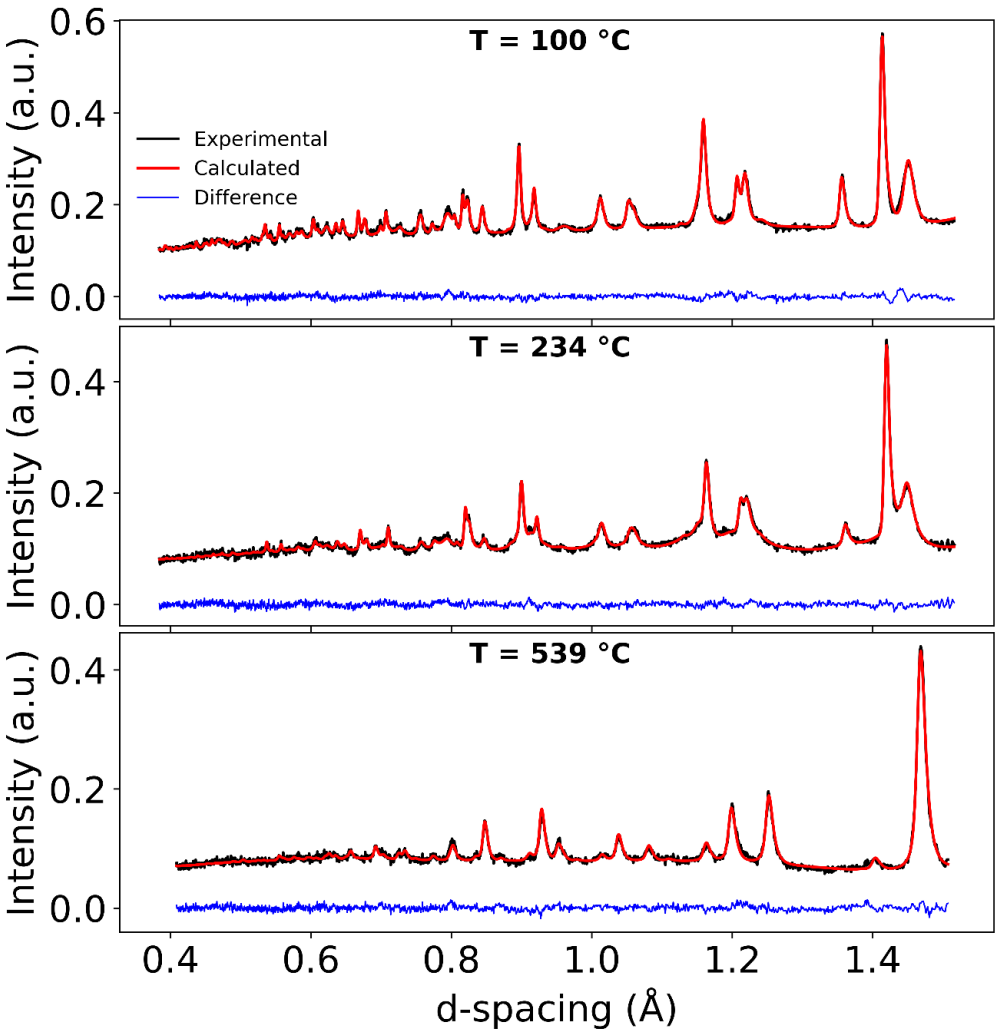


**Figure 3.** Select Rietveld refinement fits to experimental NMC333 neutron diffraction data using the initial layered structure collected at (a) 100.4 °C (Rwp= 2.859), (b) 234 °C (Rwp= 3.478), and (c) 539 °C (Rwp= 4.502). Data are given as black lines, fits as red lines, and difference curves fall below the data and fits as blue lines.

**Table 3**. Lattice parameters, atomic positions resulting from PDF refinements in range r= 5-15 Å for data set 123872 at temperature 238 °C, for layered oxide (a) a=2.837(3), c=14.198(6) with trigonal lattice, SG R $\bar{3}$m and for defect spinel with Qmax=22.

| **Atom** | **Wyck.** | **x** | **y** | **z** | **Beq, (Å$^2$).** | **Frac.** |
|---|---|---|---|---|---|---|
| | | | | | | |

**Table 3.** Continued

| | | | | | | |
|---|---|---|---|---|---|---|
| Li | 3a | 0 | 0 | 0 | 2 | 0.25 |
| Ni1 | 3a | 0 | 0 | 0.5 | 0.64(7) | 0.218(5) |
| Co | 3b | 0 | 0 | 0.5 | 0.64(7) | 0.333 |
| Mn | 3b | 0 | 0 | 0.5 | 0.64(7) | 0.333 |
| Ni2 | 3a | 0 | 0 | 0 | 0.64(7) | 0.088(7) |
| O | 6c | 0 | 0 | 0.2372(1) | 1.21(5) | 1 |

## 2.3. Results and Discussion

### 2.3.1 Average Structure Evolution from Neutron Diffraction

Operando neutron diffraction data collected during heating reveal the structural evolution of NMC333 during thermal decomposition (Figure 4). The pristine cathode adopts the layered rhombohedral structure (labelled with subscript R, space group $R\bar{3}m$). Upon heating, the layered structure gradually transforms into a disordered spinel phase (labelled with subscript S, space group $Fd\bar{3}m$) beginning near 220–230 °C. This transition is indicated by the disappearance of layered reflections such as (2–13)R and the emergence of spinel reflections including (440)S [74].

Between ~230 and 430 °C, diffraction peaks broaden and shift, reflecting increasing cation disorder and lattice distortion. Layered and spinel phases coexist in this interval, indicating a progressive transformation rather than an abrupt phase transition. Above ~430 °C, the diffraction pattern is dominated by the disordered spinel phase, consistent with extensive cation mixing and loss of long-range layered order.

The structural evolution correlates strongly with oxygen evolution measured simultaneously during the experiment (Figure 6(c)). Three oxygen-release events are observed at ~300–354 °C, ~378–424 °C, and ~454–548 °C. Oxygen loss generates oxygen vacancies that destabilize the layered lattice and facilitate migration of transition-metal ions, particularly Ni, from the transition-metal layer into Li sites. This migration promotes collapse of the layered structure and formation of the spinel framework, consistent with prior studies of thermally degraded Ni-rich layered oxides, [27], [40], [75].

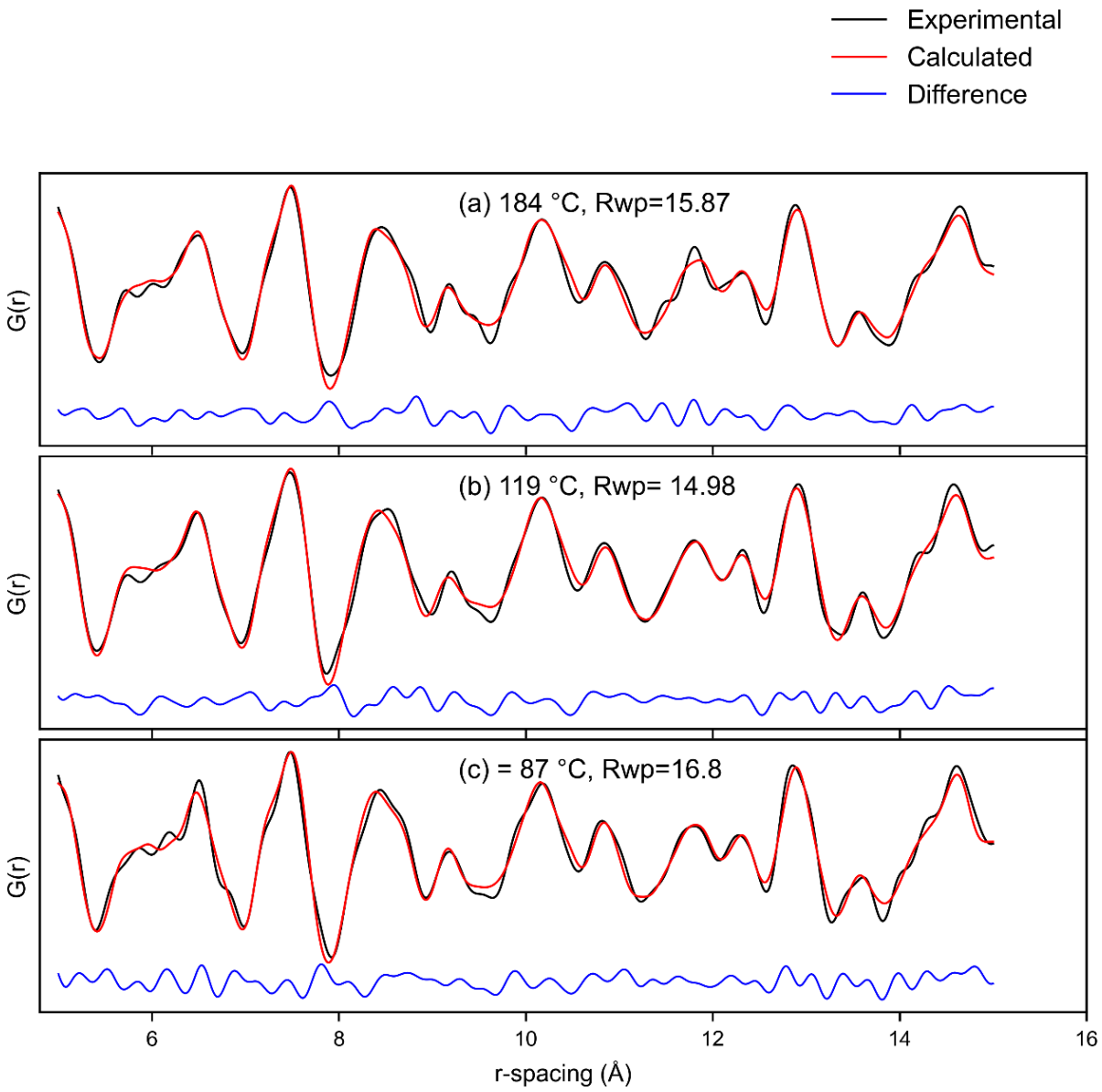


**Figure 4**. PDF fits for different temperatures with layered model in r range 5-15 Å. Selective fits to neutron total scattering data after PDF refinements for 87 °C (Rwp= 16.8), for 119 °C (Rwp= 14.98), and for 184 °C (Rwp= 15.87).

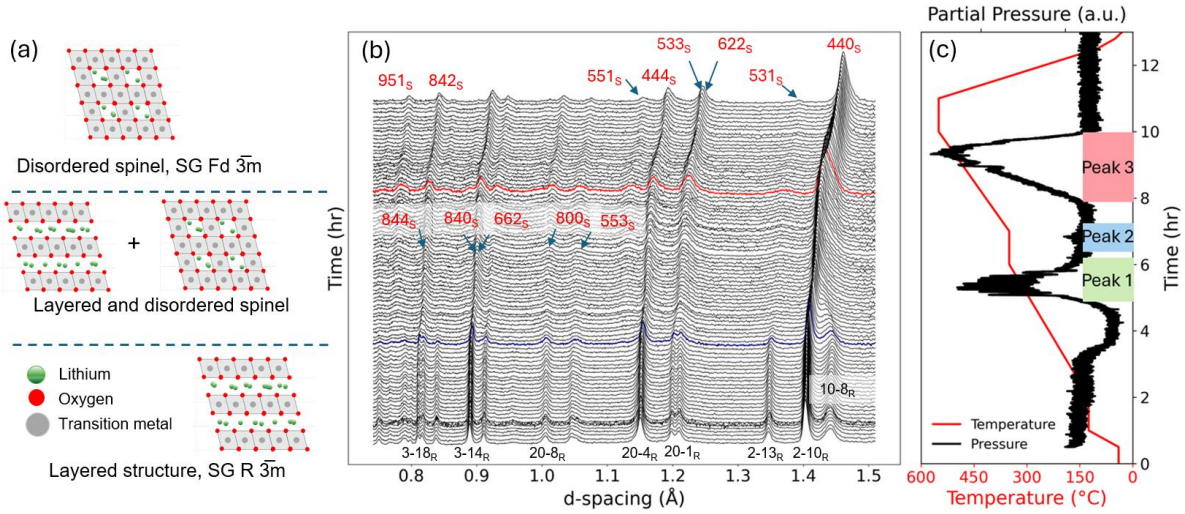


**Figure 5. (a)** Three models used to fit neutron scattering data collected from in operando thermal decomposition experiment. **(b)** Waterfall plot showing diffraction patterns collected from room temperature up to 550 °C. **(c)** Oxygen partial pressure and temperature as a function of time. The evolution of oxygen gas is closely related to phase transitions that occur during thermal decomposition.

Rietveld refinements quantify these structural changes (Figure 5). The a-axis expands with increasing temperature while the c-axis contracts between ~200–280 °C, reflecting collapse of the Li–TM interlayer spacing as Ni migrates into Li layers. Correspondingly, refined Ni occupancy on Li sites increases from approximately 0.03 to ~0.13, indicating significant antisite defect formation during decomposition.

### 2.3.2 Local Structure Evolution from Pair Distribution Function Analysis

While Rietveld refinement captures the long-range average structure, PDF analysis reveals the evolution of local atomic arrangements during heating. PDF data (Figure 6) show that layered structural motifs persist locally even after long-range ordering begins to degrade.

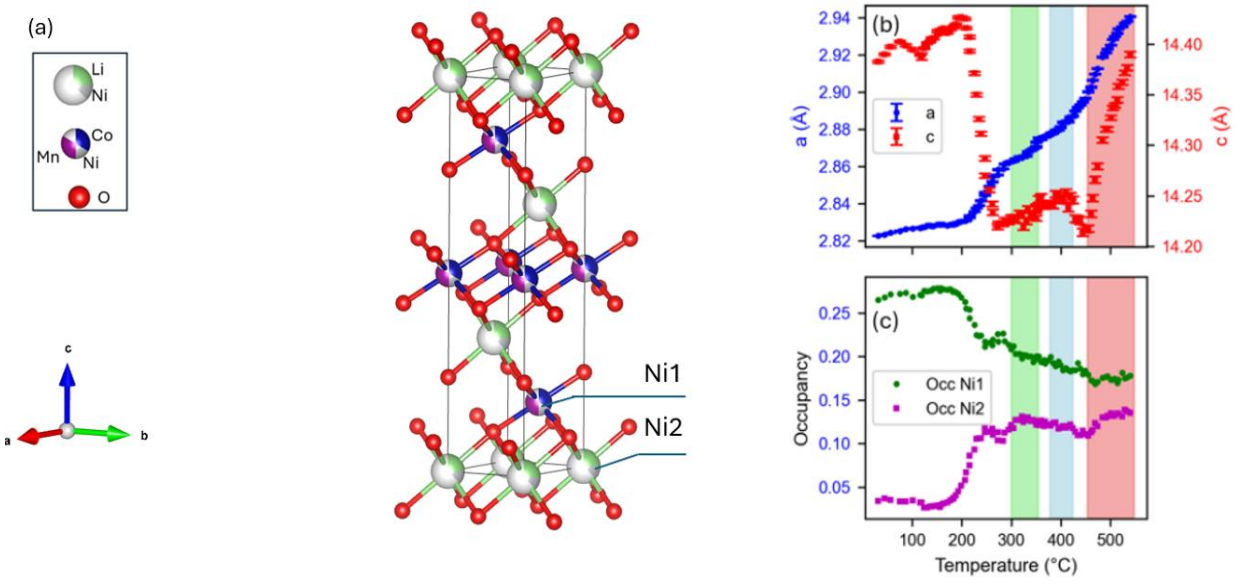


**Figure 6. (a)** Layered oxide structure (SG R$\bar{3}$m) with key characteristics labelled. 3a sites are occupied by Li and Ni. During thermal decomposition some Li ions migrate to the transition metal layer (3b sites) occupied by Co, Ni and Mn, creating increased structural disorder. **(b)** Lattice parameters a and c, and **(c)** Ni occupancy in NMC 333 from Rietveld analysis as a function of temperature. Sequential refinements were performed using the layered structure model (SG R$\bar{3}$m), which has lower symmetry compared to the disordered spinel phase (SG Fd$\bar{3}$m).

Between ~220 and 410 °C, PDF peaks broaden and decrease in intensity, particularly at higher r values (>8–10 Å), indicating increasing disorder and the emergence of short-range spinel-like environments. The persistence of distinct short-range TM–O correlations while longer-range correlations weaken suggests that local octahedral coordination remains relatively intact even as long-range layered ordering collapses.

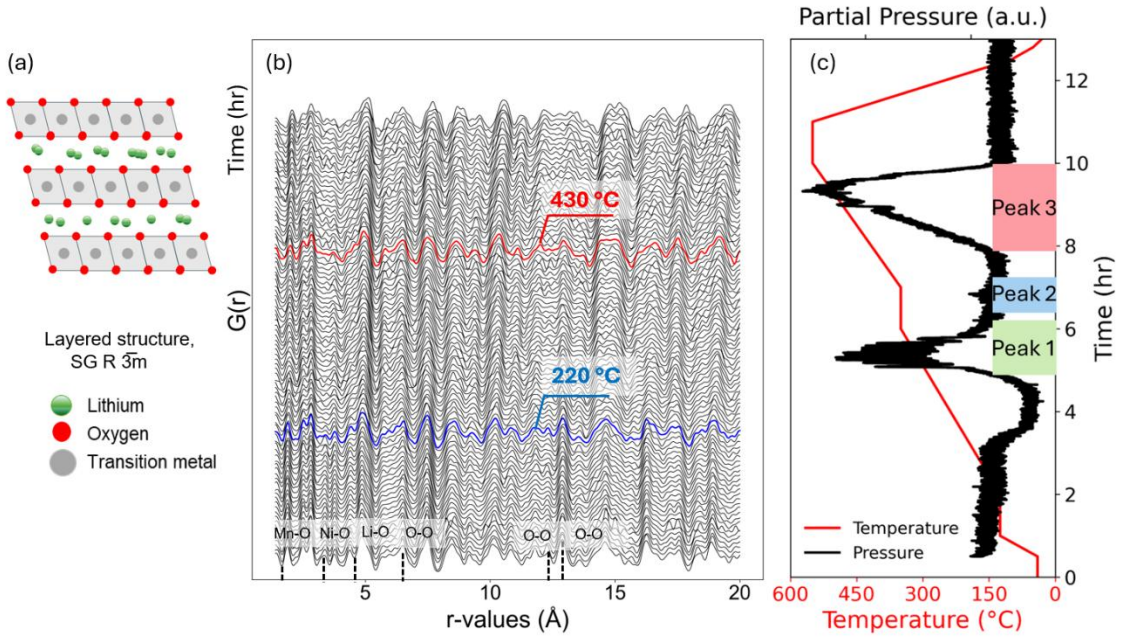


**Figure 7. (a)** Layered structure model used to fit PDF data over the entire range of the in operando thermal decomposition experiment. **(b)** Waterfall plot showing PDF patterns, G(r), collected from room temperature up to 550 °C. **(c)** Oxygen partial pressure and temperature as a function of time.

Beyond ~410 °C, mid- and long-range correlations degrade substantially, consistent with extensive oxygen vacancy formation and cation redistribution. However, TM–O bonds remain consistent at short distances, indicating that local octahedral coordination survives longer than long-range lattice order.

Refinement of PDF data in the 5–15 Å range, which probes medium-range order, confirms systematic changes in structural parameters including oxygen z-coordinate, lattice volume, and the c/a ratio (Figure 7). These parameters evolve concurrently with oxygen-release events, further supporting a strong coupling between oxygen vacancy formation and structural disorder.

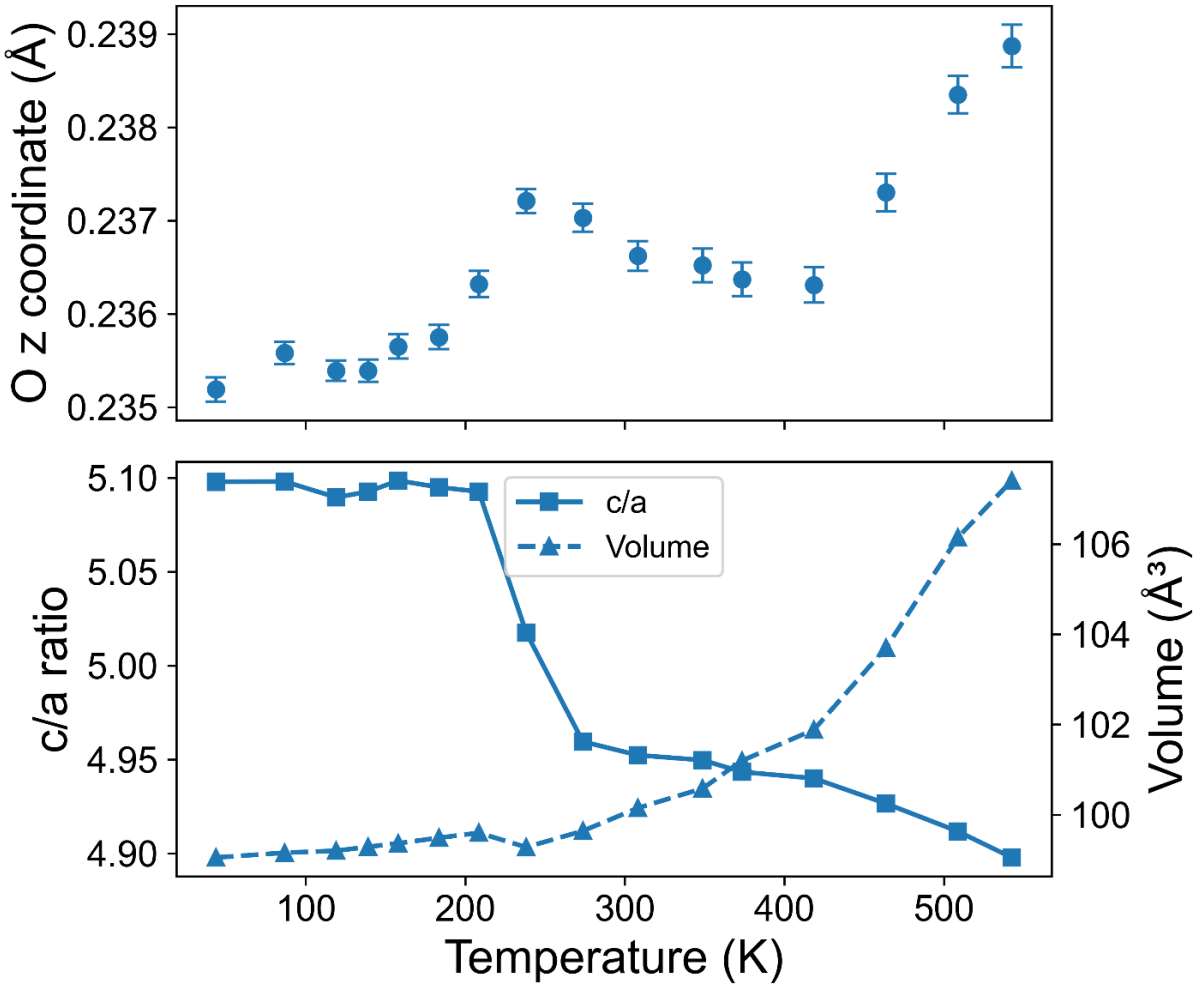


**Figure 8 (a)** z coordinate for oxygen **(b)** ratio of lattice parameters c/a and cell volume PDF refinements were performed in range r= 10-20 Å.

### 2.3.3 Multi-Scale Structural Evolution During Thermal Decomposition

Combining Rietveld and PDF analysis reveals a consistent sequence of structural transformations across length scales (Figure 10). At low temperature (<200 °C), both methods report similar structural parameters, indicating a uniformly ordered layered structure. Near ~230 °C, local structural distortions detected by PDF precede the long-range phase transition observed by Rietveld refinement. This behavior suggests that local cation migration and oxygen vacancy formation initiate structural degradation before long-range symmetry changes occur.

During the temperature range corresponding to the first two oxygen-release events (300–424 °C), layered and spinel motifs coexist. Increasing oxygen vacancy concentration reduces transition-metal oxidation states and promotes further cation migration, driving the progressive collapse of the layered framework.

Above ~430 °C, both PDF and Rietveld analyses converge, indicating that the material has largely transformed into a disordered spinel structure. [49]. Residual discrepancies between local and average structural parameters suggest the presence of nanoscale heterogeneity and oxygen-deficient domains [75].

Overall, the results demonstrate that oxygen-vacancy formation and transition-metal migration are the primary drivers of thermal degradation in NMC333, producing a layered to spinel transformation that proceeds through heterogeneous intermediate states. [48].

**2.4. Conclusions**

This work highlights the benefit of employing experimental and modeling approaches providing insight to roles that various structural and chemical parameters play to reflect structural changes and their influence on layered oxygen properties during thermal degradation. Employment of this approach allowed investigation of average structure and short-range order of layered NMC333 oxide.

This work demonstrates the advantages of combining time-of-flight neutron total scattering with operando gas analysis to directly correlate structural evolution with oxygen release during the thermal decomposition of $Li_{0.3}Ni_{1/3}Mn_{1/3}Co_{1/3}O_2$ (NMC333). This integrated approach—enabled by a newly developed high-precision gas-flow cell at SNS—allows simultaneous monitoring of long-range and local structural changes together with real-time gas evolution, offering a more complete picture of gas–solid reactivity in complex oxide materials.

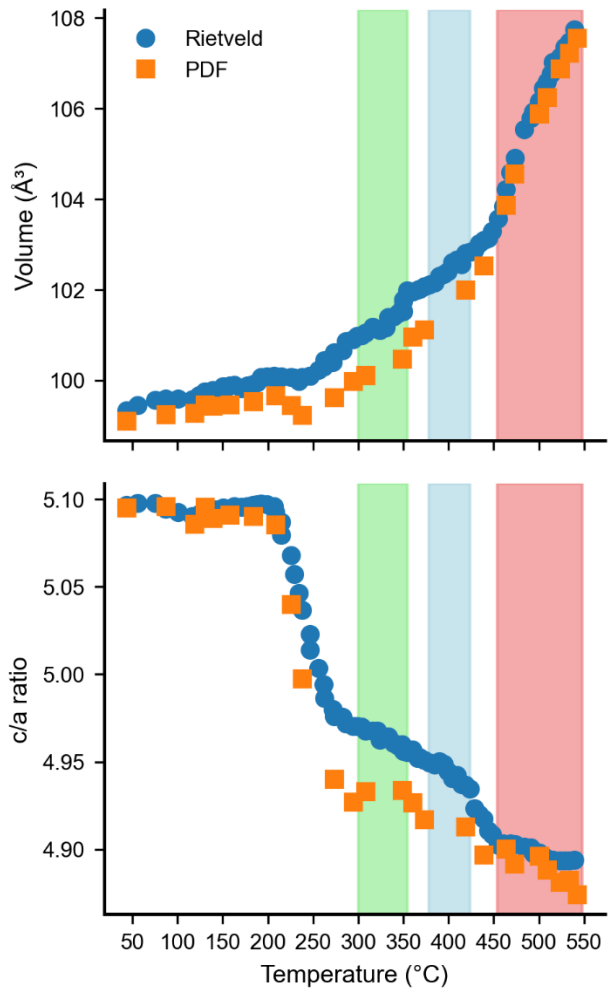


**Figure 9. (a)** Unit cell volume and **(b)** c/a ratio parameters resulting from Rietveld and PDF refinements (r=5-15 Å range) of NMC333 data collected during in situ thermal degradation. The temperature ranges corresponding to observed oxygen evolution peaks during thermal degradation are shown as solid rectangles (1st peak between 300 and 354 °C in green; 2nd peak between 378 and 424 °C in blue; and 3rd peak between 454 and 548 °C in pink).

The results reveal a clear link between oxygen evolution and cation reorganization within the layered lattice. The initial oxygen loss and Ni migration emerge near ~220–230 °C, marking the onset of the layered (SG $R\bar{3}m$) to disordered spinel (SG $Fd\bar{3}m$) transition. From ~230–430 °C, both phases coexist as antisite defects accumulate; micro strain

increases, and oxygen vacancies form as the result of first two $O_2$ release events. At ~430 °C, the layered structure is gone, and the disordered spinel becomes dominant, accompanied by increasing oxygen deficiency from the third $O_2$ release event. The multi-step oxygen-release profile reflects these structural changes during thermal decomposition of this material.

The combined Rietveld and PDF analyses highlight how total scattering captures structural dynamics across length scales: PDF identifies early local oxygen deficiency and cation rearrangement, while Rietveld refinement resolves the subsequent long-range collapse and phase transformation. Coupled with operando gas detection, this approach establishes a direct mechanistic connection between TM migration, oxygen-vacancy formation, and thermally driven phase transition.

The results suggest that material design could be improved by future investigations and might explore these strategies using bulk-sensitive structural probes (neutron diffraction, PDF), extended temperature cycling, and realistic electrode/electrolyte conditions to bridge the gap between fundamental decomposition mechanisms and practical battery safety.

Beyond insights into NMC333 degradation, this work emphasizes the broader methodological advance of integrating neutron total scattering with operando gas analysis. The new gas-flow environment enables controlled studies of gas–solid interactions under variable temperature, pressure, and gas composition, opening pathways for probing redox-driven structural evolution in energy materials, catalysts, and functional oxides. By providing a multi-scale, time-resolved view of structural responses during oxygen release, this method offers a powerful platform for understanding and ultimately mitigating thermal instabilities in Ni–Mn–Co–based cathodes and other reactive solids.

# CHAPTER THREE: MODELING LOCAL STRUCTURE IN MN-RICH DISORDERED ROCK SALT CATHODES USING PDF ANALYSIS

This chapter presents work on the family of Mn-rich cation disordered rock salt cathodes for Li-ion batteries. This material is introduced in Chapter 1, Section 1.1. This work provides a framework for understanding how the degree of local short-range order in disordered rock salt cathodes influences electrochemical performance. It also highlights the importance of examining atomic arrangements across multiple length scales when evaluating compositional effects and structural changes in these materials.

## 3.1 Introduction

Cation disordered (DRX) material is among the next generation of cathode materials in Li-ion batteries with high specific capacity and energy density. Research advancement in DRX materials has expanded the compositional design space and enabled the use of inexpensive transition metals (TM) to replace more expensive Co and Ni used in conventional cathode materials and lower cost of LIBs. DRX materials have higher specific capacity and energy than many currently used cathodes. This comparison is shown in Figure 10.

The cation sublattice in disordered rock salt (DRX) materials consists of redox-active transition metals (TMs) such as Mn, Ni, and V, redox-inactive (typically $d^0$) TMs such as Nb, Ti, and Ta, and Li cations, while the anion sublattice is composed of oxygen. In contrast to layered cathodes, DRX structures are characterized by statistical mixing of Li and TM species over a single cation sublattice. The frequently observed α-$LiFeO_2$–type structure [76] arises from such Li/TM mixing on the cation sites.

The compositional flexibility of DRX materials enables extensive tuning of electrochemical properties. For example, partial substitution of $O^{2-}$ by $F^-$ reduces the total anionic charge, which can be compensated by increasing the content of redox-active TMs or Li. The absence of long-range cation ordering significantly broadens the accessible chemical space and enables the development of high-energy cathodes with specific energies exceeding 1000 Wh $kg^{-1}$ [77].

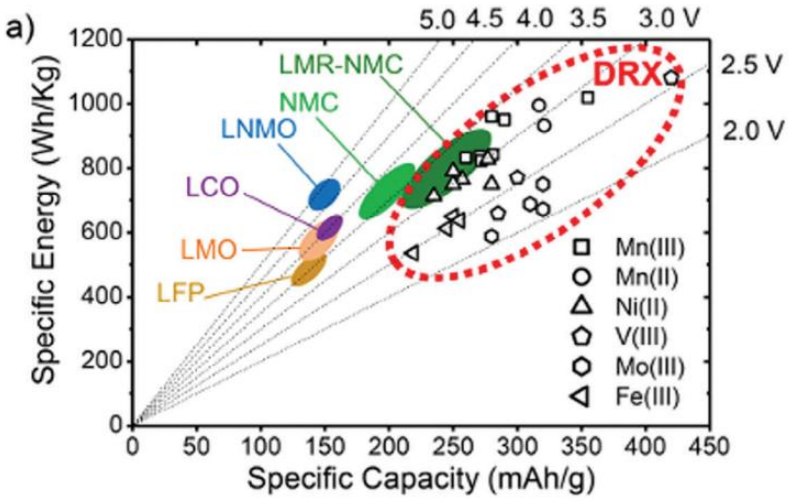


**Figure 10.** Comparison of specific energy and specific capacity of different cathode materials with those of DRXs, [76]

Although DRX materials lack long-range cation order, they exhibit short-range order (SRO), where atomic positions and site occupancies are locally correlated. Thus, DRX materials contain a distribution of distinct local chemical environments within an average rock salt lattice. [78]. As a result, DRX materials can be viewed as globally disordered structures that contain locally correlated atomic motifs.

The synthesis of DRX cathodes is challenging because formation of the thermodynamically stable γ-$LiFeO_2$ phase can occur. Unlike DRX, γ-$LiFeO_2$ is an ordered rock salt-derived structure in which Li and Fe occupy distinct sublattices. This ordering disrupts the Li percolation network, leading to isolated Li regions and poor diffusivity. In contrast, the statistical Li/TM mixing in DRX enables a percolating Li network essential for high-rate performance. The high configurational entropy associated with random occupation of the cation sublattice by Li and multiple TM species stabilizes the disordered solid solution. If γ-$LiFeO_2$ nucleates, phase separation occurs, resulting in electrochemically inactive ordered domains embedded within the DRX matrix. Incorporating high-entropy TM mixtures is therefore an effective strategy to suppress γ-$LiFeO_2$ formation and stabilize the desired disordered phase.

Fluorine doping has been widely employed to suppress γ-$LiFeO_2$–type short-range order (SRO) and improve the Li percolation network in DRX cathodes [79, 80]. Substitution of $O^{2-}$ by the more electronegative $F^-$ strengthens Li–F interactions and increases the probability of Li occupying sites adjacent to F. This promotes the formation of Li-rich clusters and enhances the connectivity of Li percolation pathways, thereby suppressing γ-$LiFeO_2$–type SRO motifs [79]. Chen et al. [81] investigated the chemical and structural evolution of F-doped DRX materials during cycling. Using $Li_{1.2}Ti_{0.4}Mn_{0.4}O_2$ (LTMO 3.0) as a baseline, they compared two oxyfluorides: Li-rich $Li_{1.3}Ti_{0.3}Mn_{0.4}O_{1.7}F_{0.3}$ (LTMOF 3.25) and Mn-rich $Li_{1.2}Ti_{0.2}Mn_{0.6}O_{1.8}F_{0.2}$ (LTMOF 2.0). Ex situ synchrotron X-ray diffraction revealed that structural evolution during cycling is driven by Mn reduction in both surface and bulk regions, accompanied by degradation of the local Mn coordination environment. Increasing fluorine content and decreasing the Li/Mn ratio were found to mitigate structural degradation, suggesting that compositional tuning through fluorination is an effective approach to enhance the cycling stability of DRX cathodes.

Accurate structural modeling is essential for quantifying SRO from diffuse scattering and pair distribution function (PDF) data. In DRX materials, both small-box (periodic unit cell) and large-box (supercell) approaches are used. Small-box models describe the average local structure but cannot fully represent the statistical variation of local environments in DRX materials. Large-box approaches are therefore needed to capture chemically correlated disorder, bond-length distributions, and local distortions more realistically.

Pair distribution function (PDF) analysis provides a direct experimental probe of these local structural variations. In DRX materials, PDF analysis is especially useful because it probes short- and medium-range atomic correlations directly. Comparison of different modeling types and the structural features they capture is summarized in Table 4.

**Table 4.** Comparison of different models for different structural aspects

| **Aspect** | **Statistical disorder** | **MC supercell** | **MC + DFT supercell** |
|---|---|---|---|

**Table 4.** Continued

| | | | |
|---|---|---|---|
| Cation occupancy | Probabilistic | Correlated | Fixed |
| Site equivalence | All equivalent | Broken | Fully broken |
| Bond lengths | Single average | Discrete set | Relaxed + split |
| SRO | None | Yes | Yes + strain |
| PDF short r fit | Poor | Better | Best |

Large-box Monte Carlo (MC) simulations have been widely applied to investigate short-range order (SRO) and Li transport in DRX materials. For example, Huiwen Ji et al.[82] combined neutron pair distribution function (nPDF) analysis, DFT, and MC simulations to study Li transport in $Li_{1.2}Mn_{0.4}Ti_{0.4}O_2$ (LMTO) and $Li_{1.2}Mn_{0.4}Zr_{0.4}O_2$ (LMZO). Their results demonstrated that three-dimensional Li percolation strongly depends on cation SRO, which modifies both the local coordination environment and the connectivity of Li diffusion pathways. This work highlights the importance of controlling local chemical order to optimize Li transport and electrochemical performance.

Nathan Szymanski et al. [83], investigated F-doped DRX materials, specifically $Li_{1.3}Mn_{0.4}Ti_{0.3}O_{1.7}F_{0.3}$ and $Li_{1.3}Mn_{0.4}Nb_{0.2}Ti_{0.1}O_{1.7}F_{0.3}$, using PDF analysis combined with MC and DFT modeling. Their study distinguished between configurational SRO (correlated cation occupations) and displacive SRO (local bond-length distortions arising from specific coordination environments). Deviations from the average rock salt structure were attributed to variations in TM–O and Li–O bond lengths caused by local chemical environments. To accurately reproduce experimental total neutron scattering data, models incorporating both configurational and displacive effects were required. The agreement between simulation and experiment validated the presence of chemically correlated local structures in F-doped DRX systems.

In DRX materials, Li diffusion proceeds via an octahedral–tetrahedral–octahedral (O–T–O) pathway within the rock salt framework (Figure 11). The migration barrier depends strongly on the local cation arrangement around the tetrahedral site, linking SRO directly to percolation and transport kinetics.

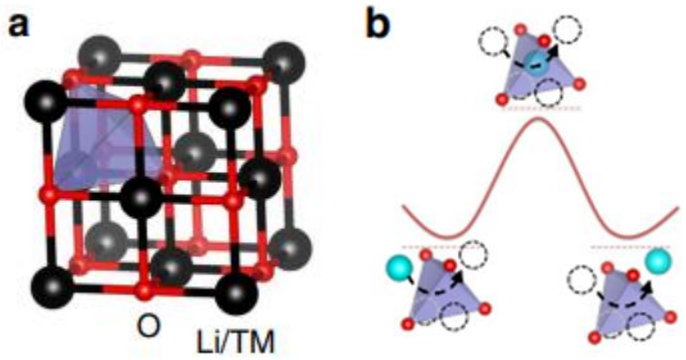


**Figure 11. (a)** Crystal structure of a cation disordered rock salt, where lithium and transition metals occupy the site depicted in black, octahedrally coordinated by red oxygen atoms. A vacant tetrahedral site is highlighted in blue. **(b)** Schematic energy landscape for migration of lithium from its octahedral site through a tetrahedral vacancy to another octahedral site [82].

Another important structural modeling approach is Reverse Monte Carlo (RMC). RMC provides a complementary large-box approach for fitting experimental total scattering data, although the resulting solutions are not unique and therefore require chemical constraints and validation.

Neutron total scattering and RMC modeling were used by Sichen Jiao et al. [84] to investigate the fluorination mechanism in $Li_{1.16}Ti_{0.37}Ni_{0.37}Nb_{0.1}O_2$ (LTNNO) and its fluorinated counterpart $Li_{1.2}Ti_{0.35}Ni_{0.35}Nb_{0.1}O_{1.8}F_{0.2}$ (LTNNOF). They found that the fraction of O–TM channels participating in the Li percolation network increased from 2.9% in LTNNO to 8.7% in LTNNOF. Fluorination promoted the merging of previously isolated Li channels into a connected percolation network, leading to improved Li-ion mobility and increased electrochemical capacity. The study emphasized the need for rational structural design strategies to enhance Li-network connectivity and control SRO for improved DRX performance.

The compositions investigated in this work were selected based on established design principles for DRX cathodes. Mn was chosen due to its high redox capacity and good reversibility in cation-disordered rock salt systems [85]. $Ti^{4+}$, a $d^0$ cation, was incorporated to stabilize the disordered framework by accommodating local strain and

promoting structural robustness [86]. The combination of Mn and Ti therefore provides a balance between high capacity and structural stability.

Fluorine doping was introduced for several key reasons. First, $F^-$ modifies short-range order (SRO) through its preferential bonding with $Li^+$, thereby influencing the local cation distribution and Li percolation network. Second, partial substitution of $O^{2-}$ by $F^-$ on the anion sublattice enhances structural and electrochemical stability during cycling [87]. Fluorination thus serves as both a chemical and structural tuning parameter in DRX materials.

In this work, we investigate the average and local crystal structures of Mn-rich cation-disordered rock salt cathodes using neutron total scattering combined with Monte Carlo (MC), density functional theory (DFT), special quasirandom structures (SQS), and special quasi-random structures for short-range order (SQoS) simulations. By fitting these models to experimental pair distribution function (PDF) data, we evaluate their ability to capture structural features across different r-ranges. Our combined experimental and computational approach provides detailed insight into cation ordering and SRO in Mn-rich DRX cathodes and clarifies how these structural characteristics influence material performance. Establishing defect–structure–property relationships in DRX systems is essential for understanding Li-ion transport during cycling and for guiding the design of high-performance, commercially viable DRX cathodes.

## 3.2 Experimental and Computational Details

### 3.2.1 Material synthesis

Four Mn-rich cation-disordered rock salt (DRX) cathode compositions were synthesized using a sol–gel method following the procedure reported by [88]. The sol–gel approach ensures homogeneous mixing of precursors at the molecular level, which is critical for achieving uniform cation distribution and stabilizing the disordered rock salt structure. Inductively coupled plasma (ICP-OES) and Fluoride Ion Selective Electrode (ISE) methods (Galbraith Laboratories Inc.) were used to measure actual atomic concentrations. The results are listed in Table 5. The experimentally determined fluorine contents were significantly lower than the nominal values. This discrepancy is attributed to flourine loss during high-temperature calcination, consistent with previous reports [89].

Samples were labeled according to their target Mn content. For example, the composition $Li_{1.14}Mn_{0.52}Ti_{0.35}O_{1.98}F_{0.01}$ is denoted as Mn0.5, where the numerical suffix reflects the target Mn content.

**Table 5.** List of materials used in this study, including compositions for one DRX oxide and three oxyfluorides with target formula $Li_{1.2}Mn_x\ Ti_{0.8-x}O_{2-y}$, (x=0.4, 0.5, 0.6, 0.7 and y=0, 0.1, 0.2, 0.3). The measured compositions are provided from ICP-OES and ISE analyses.

| Target Composition | Measured Composition | Sample Name |
|---|---|---|
| $Li_{1.2}Mn_{0.4}Ti_{0.4}O_2$ | $Li_{1.18}Mn_{0.43}Ti_{0.43}O_{1.96}$ | Mn0.4 |
| $Li_{1.2}Mn_{0.5}Ti_{0.3}O_{1.9}F_{0.1}$ | $Li_{1.14}Mn_{0.52}Ti_{0.35}O_{1.98}F_{0.01}$ | Mn0.5 |
| $Li_{1.2}Mn_{0.6}Ti_{0.2}O_{1.8}F_{0.2}$ | $Li_{1.15}Mn_{0.68}Ti_{0.24}O_{1.91}F_{0.02}$ | Mn0.6 |
| $Li_{1.2}Mn_{0.7}Ti_{0.1}O_{1.7}F_{0.3}$ | $Li_{1.14}Mn_{0.90}Ti_{0.14}O_{1.81}F_{0.02}$ | Mn0.7 |

### 3.2.2 Neutron total scattering and data analysis.

Time-of-flight (TOF) neutron total scattering measurements were performed on the NOMAD diffractometer at the Spallation Neutron Source, Oak Ridge National Laboratory [65]. Approximately 0.5 g of sample powder was loaded into a 3 mm quartz capillary. The pair distribution function, G(r), was obtained from the total scattering data. Data reduction, including normalization and merging of signals from the four detector banks, was carried out using the ADDIE software package [68].

Rietveld refinements were performed using TOPAS v6 [69] starting from an average cubic rock salt structure (space group $Fm\bar{3}m$). The refined parameters included the scale factor, peak profile parameters, lattice parameter, background coefficients, atomic positions, and isotropic atomic displacement parameters (ADPs). These refinements provided the average long-range structural model.

Experimental PDF data were analyzed using PDFgui [90] via least-squares small-box modeling. To probe disorder beyond the small-box approximation, Reverse Monte Carlo (RMC) simulations were conducted using RMCProfile [91]. A 15 × 15 × 15 supercell of the cubic $Fm\bar{3}m$ structure, containing approximately 11,000 atoms, was used as the starting configuration. Final RMC models were obtained by simultaneously fitting G(r), the total scattering structure function F(Q), and neutron diffraction patterns.

To maintain physically meaningful local environments, bond valence sum (BVS) constraints were applied during RMC simulations. The M-site cations (Li, Mn, Ti) and anions (O, F) were allowed to swap positions within their respective sublattices to model chemical disorder. Simulations were performed on a 3.2 GHz CPU core, generating more than $1.0 \times 10^7$ accepted moves over runtimes exceeding 2000 minutes. For each composition, ten independent RMC configurations were generated and used for subsequent statistical structural analysis.

Density functional theory (DFT) calculations were carried out using the Vienna Ab initio Simulation Package (VASP) [92]. A rock salt-based structural model was used as the starting configuration, and a 4 × 5 × 6 supercell was constructed. Brillouin zone sampling was performed using a 1 × 1 × 1 k-point grid. No initial magnetic moments were imposed. To better describe the localized Mn 3d electrons, a Hubbard U correction (U = 3.9 eV) was applied to Mn, improving the treatment of on-site Coulomb interactions and the accuracy of the electronic structure.

### 3.3 Results and Discussion

As introduced above, the average structure was analyzed via Rietveld refinement, confirming a long-range cubic rock salt structure (space group $Fm\bar{3}m$).. Multiple structural models were evaluated for their ability to fit the experimental PDF data, reproduce short- and medium-range correlations, and to identify the most physically meaningful description of the local structure.

#### 3.3.1 PDF analysis with disordered model

The disordered structural model used for PDF refinements was based on a single-phase cubic structure with space group $Fm\bar{3}m$, corresponding to the face-centered cubic (fcc) NaCl-type framework. PDF fits for the four compositions with the disordered model

and contribution of individual atomic pairs to the total PDF are shown in Figure 12. Although the $Fm\bar{3}m$ model adequately captures the long-range average structure, deviations from the ideal NaCl-type arrangement are evident in the experimental PDF data. Peak broadening, asymmetry, and slight shifts in first- and second-neighbor correlations indicate local distortions of the $MO_6$ octahedra and the presence of chemical short-range order (SRO). Because $Li^+$, $Mn^{3+}$, and $Ti^{4+}$ differ in ionic radius and charge, their statistical occupation of the cation sublattice introduces local strain and bond-length variability that are not fully described by the average cubic symmetry. Thus, the single-phase disordered model serves as a useful baseline, but it does not capture the full extent of local structural heterogeneity.

### 3.3.2 PDF analysis with biphasic model

PDF refinements of the neutron total scattering data using a biphasic structural model provided the best agreement with the experimental G(r) at low r. The model includes $LiMnO_2$ and $Li_2TiO_3$ components and suggests the presence of locally Mn-rich and Ti-rich environments within the nominally disordered rock salt framework.

The monoclinic m-$LiMnO_2$ structure belongs to the space group C2/m and adopts a layered α-$NaFeO_2$–type framework. It consists of alternating Li and $MnO_2$ slabs derived from a cubic close-packed oxygen lattice. $Mn^{3+}$ ions occupy octahedral sites within the $MnO_2$ layers, while $Li^+$ ions reside in octahedral sites between these layers. The layers are oriented parallel to the (111) planes of the cubic oxygen sublattice, and both Li and Mn cations are coordinated by six oxygen anions [93]. The second component, $Li_2TiO_3$, crystallizes at room temperature in a monoclinic structure (space group C2/c), commonly described as a layered silverite-type framework. Both $Li^+$ and $Ti^{4+}$ ions are octahedrally coordinated by six oxygen atoms, forming $LiO_6$ and $TiO_6$ octahedra. The structure contains two crystallographically distinct Li sites and one Ti site, along with two inequivalent oxygen sites. Octahedra are interconnected via corner-sharing and edge-sharing interactions: $LiO_6$ octahedra share corners with $TiO_6$ and neighboring $LiO_6$ units, while $TiO_6$ octahedra share corners with both adjacent $TiO_6$ and $LiO_6$ octahedra. Edge-sharing occurs between $LiO_6$–$TiO_6$ pairs and between neighboring $LiO_6$ octahedra [94]. $Li_2TiO_3$ may exhibit stacking faults within the Li–Ti layers, giving rise to short-range

order (SRO) effects. These structural defects can locally alter the connectivity of octahedral pathways, potentially influencing lithium-ion mobility [95].

Incorporating both $LiMnO_2$ and $Li_2TiO_3$ phases in the PDF modeling accounts for the presence of locally ordered Mn-rich and Ti-rich domains within the nominally disordered rock salt matrix. This biphasic approach provides an improved representation of the short- and medium-range correlations observed in the neutron PDF data, but it is inconsistent with the long-range cubic rock salt average structure.

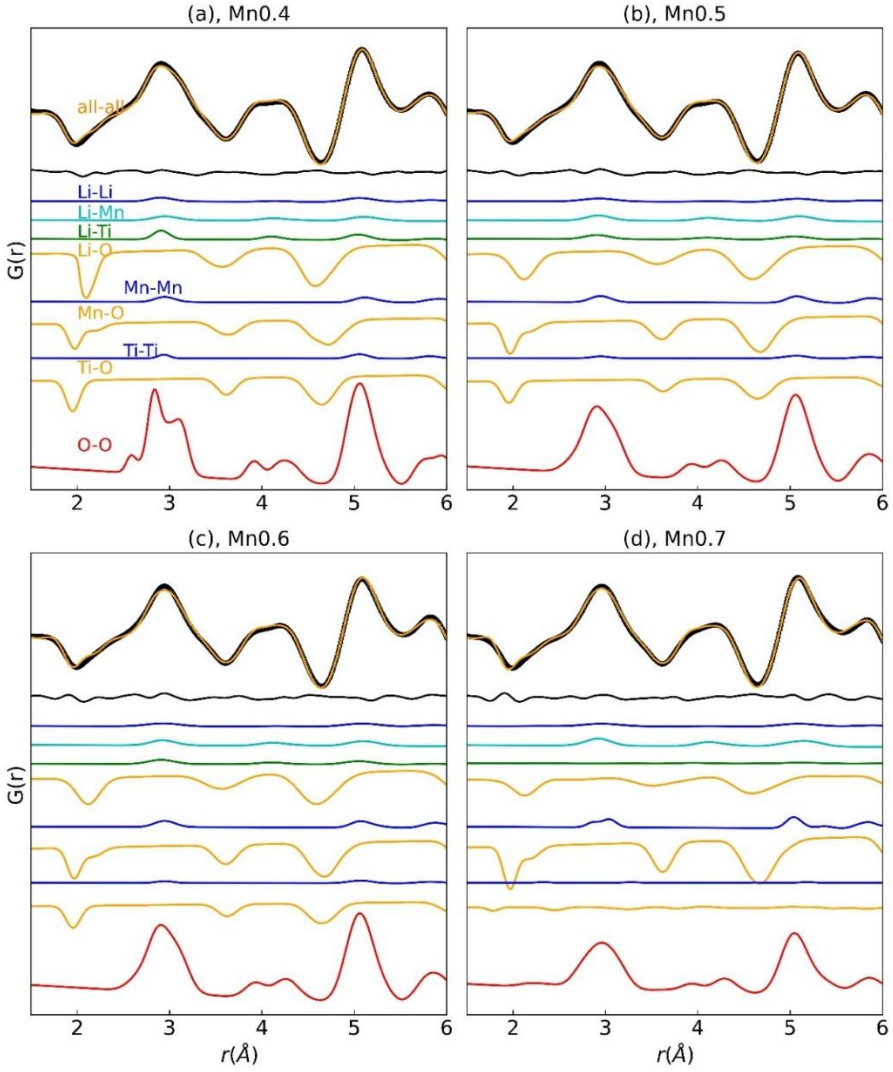

**Figure 12**. Calculated PDF fits and corresponding partial PDFs for disordered rock salt (average structure) model fits to data from the four compositions over the PDF r-range 1.5-6 Å.

### 3.3.3 PDF analysis with MC-DFT (GGA and SCAN) models

The large-box Monte Carlo (MC) simulations, followed by DFT relaxations, generated statistically meaningful ensembles of disordered rock-salt (DRX) configurations that capture local cation correlations and structural distortions more realistically than the average disorder model. The use of a 4 × 5 × 6 supercell (240 atoms), shown in Figure 13, ensured proper sampling of medium-range correlations and minimized artificial periodicity effects present in smaller cells.

Two exchange–correlation functionals were employed: GGA [96], and SCAN [97]. While GGA provides a widely used gradient-corrected approximation, SCAN incorporates additional dependence on the kinetic energy density and satisfies a broader set of exact constraints, generally yielding improved descriptions of local bonding and transition-metal–oxygen interactions. Comparison of these funcationals allows evaluation of the sensitivity of local distortions and PDF agreement to the choice of DFT treatment.

During PDF refinements of the DFT relaxed models in PDFgui, only the lattice parameter *a* was refined, with *b* and *c* constrained via fixed b/a and c/a ratios. Tests with different initial atomic displacement parameters showed negligible effects on the final $R_w$ values. The fixed parameters selected for final model fitting of the Mn0.4 composition are given in Table 7. As an example, results (Rw values) of refinement using 100 GGA relaxed model configurations for fitting of Mn0.4 PDF data, are presented in Figure 14. The distribution of $R_w$ values across the 100 structure ensembles indicates that multiple local configurations can describe the data reasonably well, as expected for a disordered system. This analysis was completed for all compositions. In the case of SCAN relaxed configurations, more than 15 configurations were included in analysis for each composition, with the best selected for further data analysis.

This strategy enabled objective selection of the five lowest-Rw structures for each composition for detailed analysis. Because occupancies were fixed and no vacancies were

included, variations in Rw among models arise solely from differences in short-range cation arrangements and associated bond distortions. Therefore, the refinement results provide direct insight into how local cation ordering and functional choice influence PDF agreement. The distribution of Rw values across the 100 GGAstructure ensembles also reflects the extent of configurational space sampled by MC and subsequently relaxed via DFT.

Overall, this workflow—large-box MC → DFT relaxation → constrained PDF refinement—enables a systematic assessment of structural realism across statistically significant ensembles. It ensures that the selected models are not artifacts of a single configuration but represent energetically plausible and experimentally consistent realizations of the disordered DRX structure.

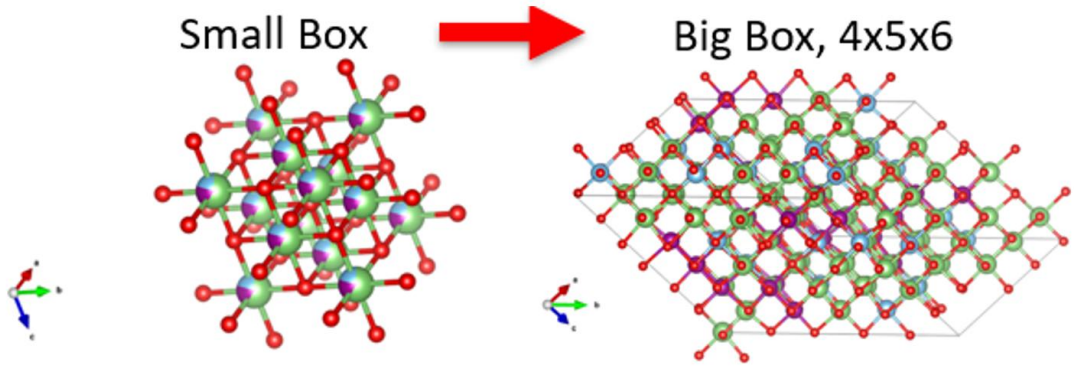


**Figure 13.** Schematic for small and big box modelling.

**Table 6.** List of parameters used to refine structures obtained from MC-DFT models within PDFgui to test moxel structures against experimental data.

| Parameter | Initial | Fixed |
|---|---|---|
| Phase Scale | 0.118 | Yes |
| Peak Width Correlation, $\delta_2$ (Å$^{-2}$) | 0.5 | Yes |
| ADP, metals (Å$^2$) | 0.005 | Yes |
| Lattice Parameter, a, (Å) | 11.785 | No |
| ADP, oxygen (Å$^2$) | 0.004 | Yes |

A comparison of refinements for the Mn0.4 composition data using different structural models—(1) single-phase statistically disordered average structure, (2) biphasic model, (3) MC–DFT (GGA), and (4) MC–DFT (SCAN)—over two r-ranges (1.5–12 Å and 1.5–25 Å) is summarized in Figure 15. For the extended r-range (1.5–25 Å), the single-phase disordered model provides the best overall agreement.

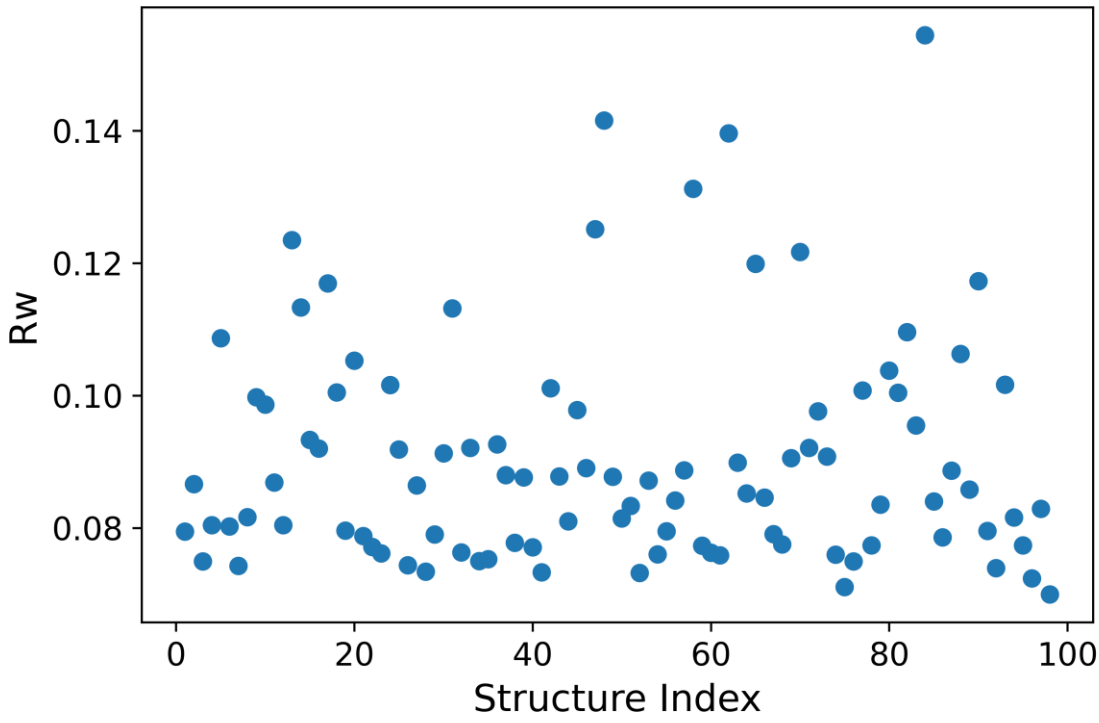


**Figure 14.** Rw resulting from PDF refinement of Mn0.4 data using 100 different structure models relaxed with a DFT GGA functional - MC-DFT(GGA).

In the short- and medium-range region (1.5–12 Å) the biphasic model offers an improvement. However, the MC–DFT models provide the best agreement overall and they explicitly capture local distortions and cation correlations within an overall rock salt ordered framework.

Overall, the range-dependent refinement behavior highlights an important structural distinction:

- **Long-range PDF fits** are governed primarily by average crystallographic order.

- **Short-range PDF fits** are governed by local distortions and short-range cation ordering.

Thus, better fits in the 1.5–12 Å region indicate superior modeling of local structure and SRO, whereas better fits in the 1.5–25 Å region reflect accurate reproduction of the average periodic framework. This comparison demonstrates that no single model universally outperforms the others; rather, each capture different structural length scales within the disordered system. Overall, the refinement behavior is strongly length-scale dependent: long-range fits are governed primarily by the average structure, whereas short-range fits are controlled by local distortions and short-range cation ordering.

### 3.3.4. PDF analysis with SQS-DFT model

In SQS–DFT modeling, the cation distribution is constructed to reproduce the correlation functions of an ideal random alloy [98].

Subsequent DFT relaxation minimizes the total energy with respect to atomic positions and lattice parameters, relieving local strain and adjusting bond lengths and angles. SQS–DFT therefore represents a locally relaxed but statistically random structure, in contrast to MC–DFT models that allow short-range order to emerge through configurational sampling.

Two SQS supercells were constructed with sizes of 4 × 4 × 5 and 5 × 6 × 6. After building these SQS structures, DFT relaxations were performed using the GGA functionals to obtain SQS–DFT structures, which were subsequently refined using PDFgui. PDF refinements indicate that the larger 5 × 6 × 6 supercell with GGA provides better agreement with experimental PDFs, and this model was used for further analysis. The results of refinements over the r-range 6–25 Å for the four compositions are presented in Figure 16.

### 3.3.5. PDF analysis with SQoS-DFT model

In addition to the SQS-based models, the Special Quasi-ordered Structure (SQoS) approach was employed, followed by DFT relaxation (SQoS–DFT). In contrast to SQS structures, SQoS structures intentionally incorporate controlled short-range order (SRO) motifs prior to DFT relaxation. This is achieved using correlation functions, which

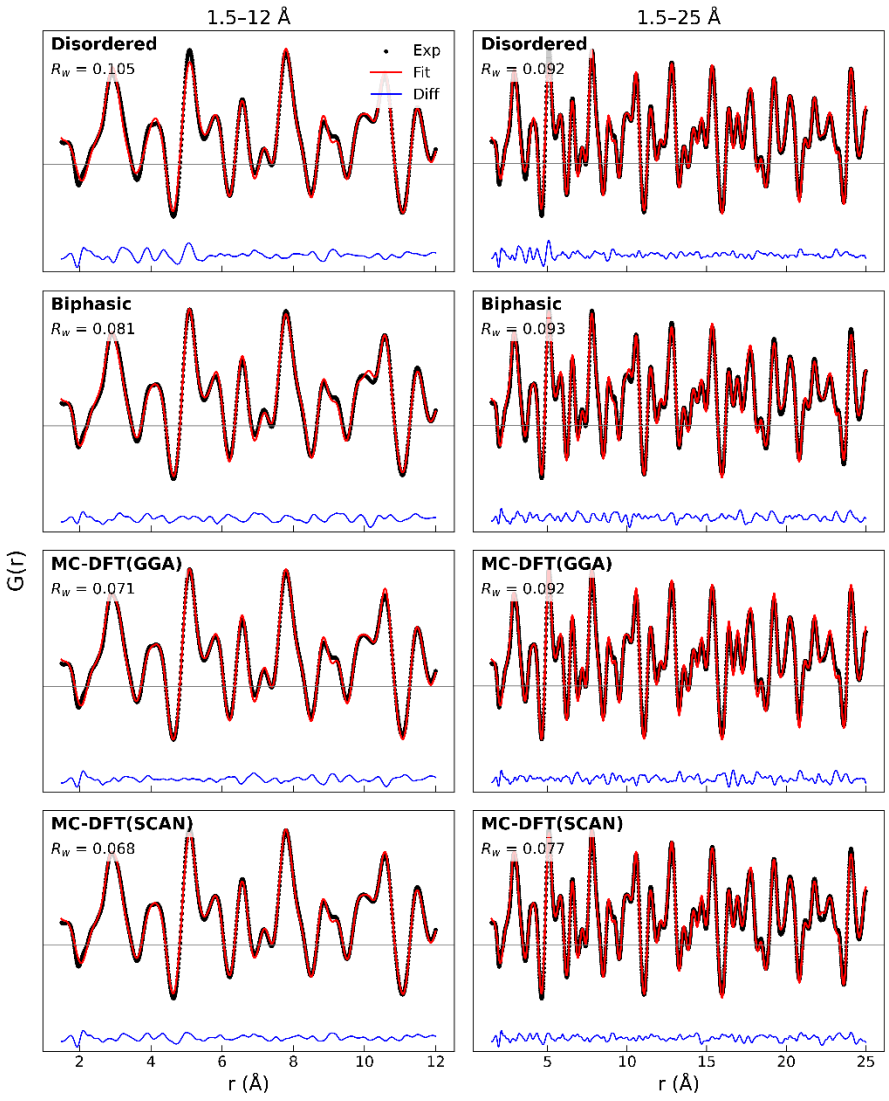


**Figure 15.** Comparison of PDF fits using different models for Mn0.4 data. The left column of figures shows PDF refinements in the range of 1.5-12 Å, while the right column of figures shows refinements in the range of 1.5-25 Å.

quantitatively describe how atomic occupations are spatially correlated across different coordination shells. These correlation functions originate from the cluster's expansion formalism, where each lattice site is mapped onto an occupation variable, and structural order is described through averages of products of these variables over defined clusters. In SQoS, selected correlation functions are deliberately deviated from their random

values to isolate specific motifs. For example, increasing the 1NN Li–Li pair correlation promotes Li clustering, while enhancing Li–TM pairing enforces cation mixing. By tuning specific shells (e.g., 1NN or 2NN), local SRO is captured without imposing long-range order.

Thus, SQoS–DFT serves as an intermediate model between purely statistical disorder (SQS–DFT) and the fully configurationally evolved structures obtained from Monte Carlo sampling followed by DFT relaxation (MC–DFT). Compared to SQS–DFT, SQoS–DFT enables targeted evaluation of energetically favorable cation arrangements, such as preferred Li–TM separations or Mn-rich clustering, while maintaining overall compositional homogeneity. Relative to MC–DFT, which explores a broad configurational space guided by a thermodynamic Hamiltonian, SQoS–DFT tests specific local ordering hypotheses in a more constrained manner. supercells (4 × 4 × 5 and 5 × 6 × 6) were constructed for SQoS. DFT relaxations using both GGA and SCAN functionals were performed to obtain SQoS–DFT structures which were subsequently fitted to experimental PDF. The SQoS–DFT structure using 5 × 6 × 6 super cell with GGA functional yielded the lowest Rw value in all compositions, except for $Mn_{0.6}$, where the 4 × 4 × 5 supercell with the GGA functional provided the best fit. These structures were subsequently selected for range-dependent refinements over the 6–25 Å $r$-range, with the results presented in Figure 16.

**3.3.6. Range-dependent refinements and violin plots**

Real-space range-dependent refinements, evaluating the goodness-of-fit achieved for a model over a specific real-space window ($r_{min}$ to $r_{max}$), can be used to quantitatively compare the utility of various models for describing local structure features found at different length scales. Figure 16 shows results of range-dependent PDF refinements (Rw vs $r_{max}$) for the four DRX compositions using the different local structure models described above to fit the data. Refinement quality, quantified by Rw, reveals trends with composition and highlights which r-ranges are well or poorly described by the various modeling approaches explored.

Short-range order (SRO), typically <5–6 Å, captures nearest-neighbor bonds (TM–O, Li–O) in the first and second coordination shells. This region provides

sensitivity to local bond-length variations, octahedral distortions, and local effects such as Jahn-Teller distortions. Medium-range order (MRO), ~5–6 Å to 15–20 Å, reflects correlations beyond nearest neighbors, including octahedral connectivity, cation clustering, and local structural motifs spanning multiple unit cells. Long-range order (LRO) extends beyond ~20 Å and corresponds to periodic crystallographic order, which is primarily captured by Rietveld refinement.

Range-dependent PDF refinements show that deviations between structural models increase systematically with Mn content and r-range.

For low Mn content (Mn0.4), MC-DFT(GGA) and MC-DFT(SCAN) models outperform the disordered model across the entire r-range. Beyond ~30.5 Å, the disordered model becomes better than MC-DFT, reflecting weak local ordering and a relatively uniform network. For moderate Mn content (Mn0.5 and Mn0.6), MC-DFT models perform better over most of the range explored, with the disordered model becoming better than MC-DFT at greater than ~20–23 Å. At the highest Mn content (Mn0.7), where the TM sublattice is Mn-dominated, the disordered model becomes more competitive and outperforms MC-DFT in goodness-of-fit at greater than ~19 Å.

Overall, MC–DFT configurations (relaxed GGA and SCAN) consistently yield the lowest Rw values across the full r-range, indicating that energetically minimized cation arrangements best reproduce experimental correlations. Although MC-DFT models provide the most physically realistic description of the local structure, they are computationally demanding because they require extensive configurational sampling followed by first-principles relaxation. In comparison, SQS-DFT and SQoS-DFT approaches offer computationally more efficient alternatives that capture many key features of the disordered framework, particularly at intermediate and longer length scales. However, these approaches do not reproduce the full extent of local structural relaxation and emergent cation correlations as accurately as the MC-DFT models.

The correlation length, $\xi$, defined by the crossover in goodness-of-fit between the small-box and the MC-DFT large-box models, connects the extent of atomic disorder to the Li percolation network. Effect of Mn content on size of locally ordered regions is shown in Figure 17. Correlation length varies monotonically with Mn content. The

correlation length reflects the spatial extent of local cation arrangements captured by the model. In DRX materials, Li diffusion depends on the connectivity of channels favorable for Li diffusion (Li reach tetrahedral environments). Mobility of Li depends on how many tetrahedral sites are surrounded by Li instead of transition metals. A decrease in correlation length therefore suggests a reduced spatial continuity of local environments effecting Li percolation network.

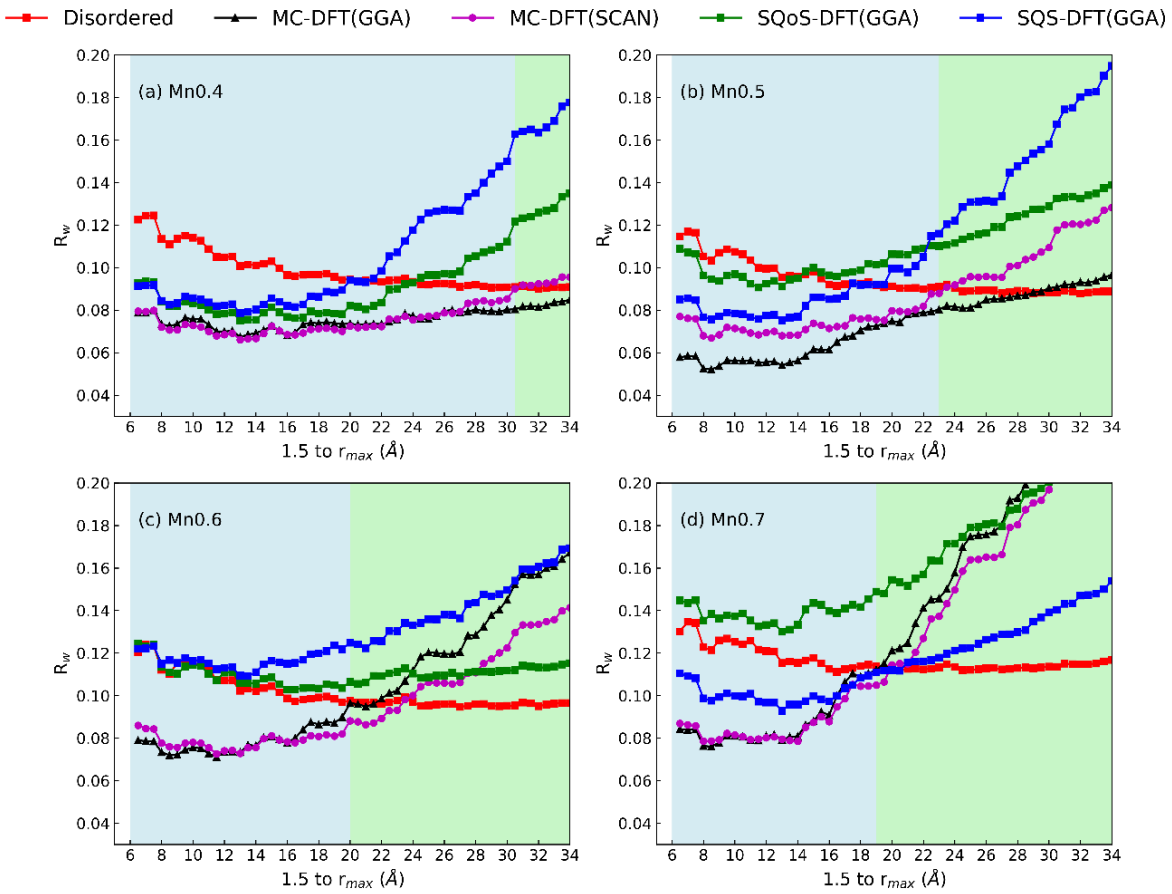


**Figure 16.** Goodness-of-fit results for range-dependent PDF refinements of data from four DRX compositions (a)-(d). There were five models used for refinements: (1) the disordered rock salt model (red symbols); and (2-5) the four big box models MC-DFT(GGA) (black symbols), MC-DFT(SCAN) (purple symbols), SQS-DFT(GGA) (blue symbols), and SQoS-DFT(GGA) (green symbols). The correlation length, ξ, defined by the crossover in goodness-of-fit between small-box and the best-performing MC-DFT based-models, is indicated in the transition between blue and green shading.

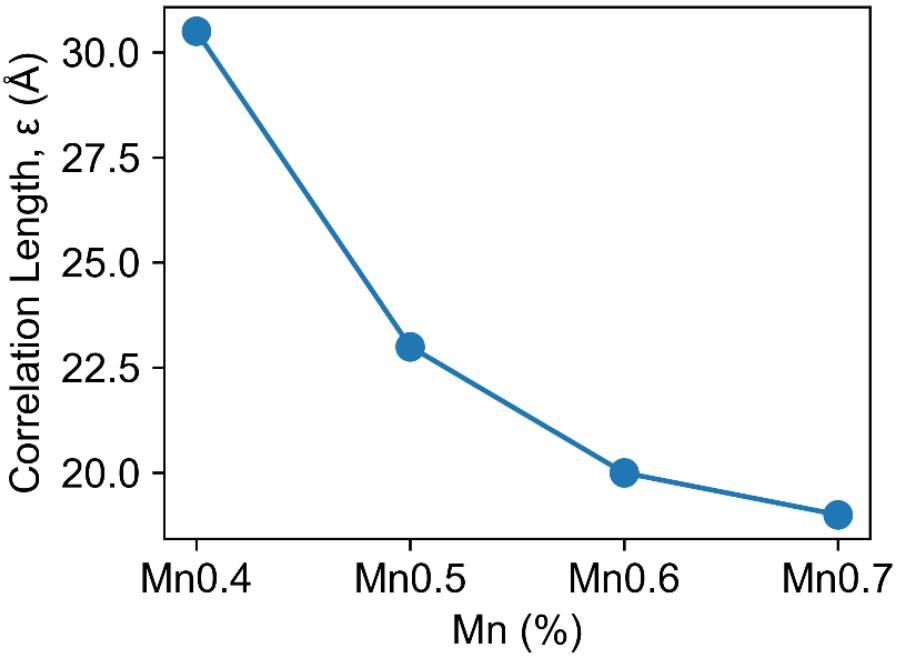


Figure 17 Correlation length as the function of Mn content from analysis with car box PDF refinements up to 34 Å for 5 different models.

Violin plots were used to visualize the distributions of local bond lengths from MC–DFT(GGA) DRX supercells, shown in Figure 18. These plots capture a direct comparison of local distortions across the four compositions, illustrating how cation disorder and local chemical environments influence short-range structure in DRX cathodes.

In Ti–O violins, shown in Figure 18(a) the average bond length (BL) remains ~2.0 Å for the first three compositions, increasing slightly to ~2.035 Å in Mn0.7. The Ti-O distribution remains relatively constant and narrow for the first three compositions, indicating the $TiO_6$ framework is rigid. A slighter greater spread in Ti-O distances is seen for the Mn0.7 compositions, as Ti becomes a minor component in the lattice.

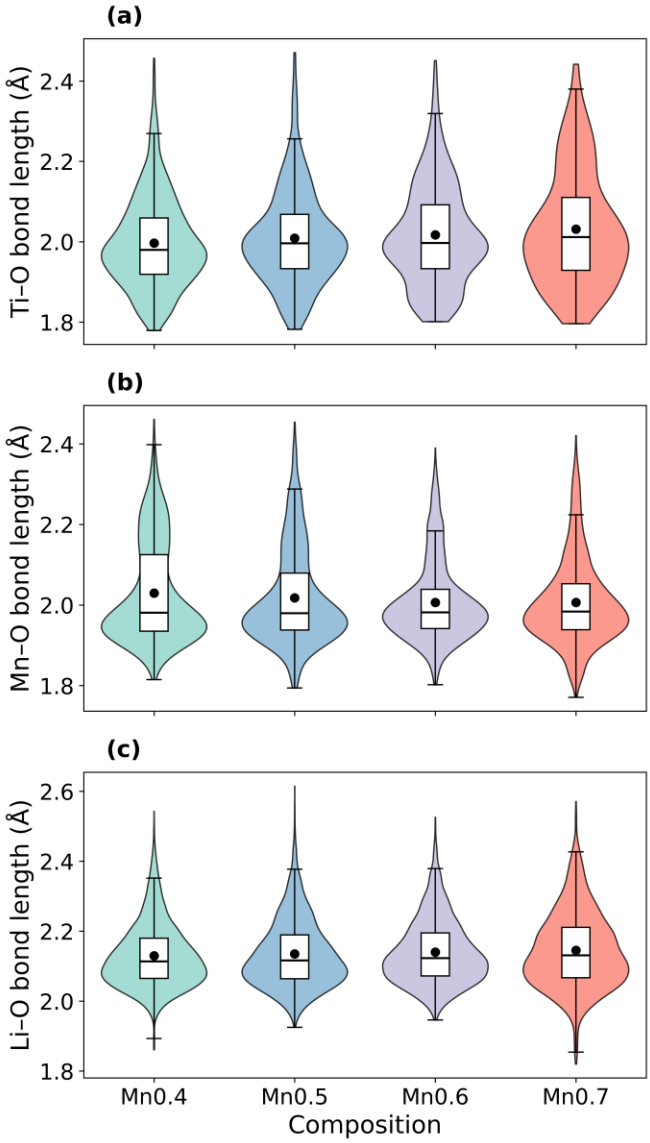


**Figure 18.** Violin plots show the distribution of bond lengths for (a) Ti-O, (b) Mn-O, and (c) Li-O resulting from MC-DFT(GGA) PDF modeling over the r-range of 1.5-12 Å. In each case, the bond length distributions are taken from the five best model fits (those resulting in the five lowest Rw values) out of 100 candidate structure models.

For Mn–O violins, the widest spread and most asymmetry occurs in Mn0.4, where Mn is the minor transition metal component. Increasing the Mn content reduces multimodality and formation of local domains with increaed Mn shows increased $MnO_6$

symmerty. A slight deacrease in average Mn-O bond length is seen with the increase in Mn content.

Li–O violins show an average bond length of ~2.1 Å across all compositions. In Mn0.7, however, the quartile box is tallest, indicating more heterogeneous Li–O distances due to altered Li/Mn short-range order. The broader Li-O distributions indiciate increasing variability in local Li coordination environments, which is expected to influnce Li transport. Such heterogenity leads to a wider distribution of Li site energies and migration barriers since there is a coexistence of channels favorable to Li diffusion and regions with blocked Li diffusion. This heterogenity tends to provide less efficient Li transport compared to compositions with narrower Li-O distributions. Concurrently, the reduction in correlation length suggests that structural correlations become increasingly short-ranged. Together, these trends might point to a fragmentation of the Li diffusion network, where locally diverse environments are not sustained over long distances. As a result, Li transport is likely governed by spatially heterogeneous and weakly connected pathways in high Mn composition, rather than a well-percolating network observed in lower Mn compositions.

### 3.4. Conclusions

Neutron total scattering and PDF analysis show that Mn-rich disordered rock salt cathodes are best described as globally disordered materials with composition-dependent local structural correlations. While all compositions retain an average cubic rock salt framework, deviations in the low-r PDF region demonstrate that the local structure cannot be adequately captured by a purely statistical small-box model.

Among the structural models examined, large-box MC-derived configurations followed by DFT relaxation, MC-DFT, provide the most accurate description of the local structure across the short- and medium-range PDF regime. These relaxed models reproduce the experimental peak positions, broadening, and asymmetry more effectively than either the average disordered model or simplified large-box approaches, confirming that local cation correlations and bond-length distortions are essential features of the DRX structure. The crossover between large-box MC-DFT and the disordered model fits further indicates a finite structural correlation length that varies monotonically with Mn content, consistent with composition-dependent degrees of correlated disorder.

Analysis of bond-length distributions from the lowest- $Rw$ relaxed MC-DFT(GGA) structures provides additional insight into the origin of this local heterogeneity. Ti–O bond length distributions remain relatively constant across the series, indicating that $TiO_6$ octahedra form a comparatively rigid local framework. In contrast, Mn–O and Li–O bond distributions are broader and more asymmetric. Increased Mn content reduces multimodality in Mn–O bonds, reflecting partial homogenization, whereas Li–O distributions broaden and become more asymmetric, highlighting the influence of local $MnO_6$ distortions on Li coordination. Together with the trend of the decrease in correlation length with increased Mn content, these trends suggest fragmentation of Li diffusion network with weakly connected pathways in high Mn composition. It negatively impacts Li diffusion pathways and contributes to the composition-dependent transport behavior of these materials.

Overall, this work demonstrates that a multiscale structural modeling framework is essential for understanding Mn-rich DRX cathodes. Accurate representation of both local bond distortions and correlated cation disorder is critical for establishing structure-property relationships and guiding the design of improved high-capacity cathode materials.

## CHAPTER FOUR: CONCLUSIONS AND RECOMMENDATIONS

This thesis presents an integrated experimental and computational investigation of layered NMC333 ($Li_{0.3}Ni_{1/3}Mn_{1/3}Co_{1/3}O_2$) and Mn-rich cation-disordered rock salt (DRX) cathodes, elucidating structural dynamics, cation disorder, and their impact on Li-ion transport and thermal stability.

In chapter two on layered NMC oxides, time-of-flight neutron total scattering, combined with operando gas analysis, reveals the mechanistic link between structural evolution and oxygen release. Oxygen loss begins near 220–230 °C, triggering Ni migration and the onset of the layered-to-disordered spinel transition. Multiple $O_2$ release events between 230–430 °C coincide with antisite defect formation, micro strain accumulation, and oxygen vacancies, culminating in a fully disordered spinel at ~430 °C. PDF and Rietveld analyses provide complementary insights: PDF captures early local cation rearrangements and oxygen deficiencies, while Rietveld resolves the subsequent long-range structural collapse. This multi-scale, time-resolved approach establishes a direct connection between transition-metal migration, oxygen-vacancy formation, and phase transformation.

In chapter three on Mn-rich DRX cathodes, neutron total scattering combined with PDF analysis and both small-box and large-box modeling (disordered average structure, biphasic model, MC–DFT, SQS-DFT and SQoS–DFT) demonstrates that cation disorder is composition-dependent and exhibits correlated behavior rather than purely random occupation. Car box refinements reveal a crossover point between the small-box disordered model and large-box relaxed models, defining a correlation length which varies monotonically with Mn content: ~30.5 Å at low Mn (weak but long-range correlations), ~20–23 Å at intermediate Mn (strong local order frustrated by competing interactions), and ~19 Å at high Mn (more coherent propagation in a Mn-dominated sublattice). Large-box MC–DFT models consistently reproduce the short- and medium-range structural correlations better than the average disordered model, emphasizing the importance of capturing local configurational heterogeneity.

Violin plots of Ti–O, Mn–O, and Li–O bonds further illustrate local structural heterogeneity. $TiO_6$ frameworks remain rigid across compositions, while Mn–O and Li–

O distributions reveal Jahn–Teller distortions, short-range chemical correlations, and cation disorder. Increased Mn content reduces Mn–O multimodality, indicating partial alleviation of local distortions, while Li–O distributions broaden and become more asymmetric, reflecting the impact of local $MnO_6$ distortions on Li coordination and percolation pathways. These local variations correspond to trends in Rw values from PDF refinements, confirming that short-range order and correlated disorder dominate local structural behavior even in the absence of long-range periodicity.

Across both cathode systems, structural behavior at multiple length scales dictates functional performance. In NMC, local oxygen deficiencies and cation migrations precede long-range collapse and oxygen release. In DRX cathodes, correlated disorder and short-range cation motifs govern Li diffusion despite the absence of long-range order. The correlation length connects atomic-scale disorder to Li diffusion which is important for functional properties of LIBs.

We suggest the following recommendations:

1. Employ multi-scale experimental probes (neutron diffraction, PDF, operando gas analysis) to capture local and long-range structural dynamics under realistic battery conditions.
2. For DRX materials, tailor short-range order through doping and controlled synthesis to optimize Li percolation pathways while mitigating configurational frustration.
3. Use combined small-box and large-box modeling approaches to quantify correlation lengths and local heterogeneity.
4. For layered NMC cathodes, explore dopant engineering and synthesis optimization to reduce oxygen loss and improve high-temperature stability.
5. Extend this integrated experimental–computational framework to other complex oxide or high-entropy cathodes to guide the rational design of high-performance, thermally stable battery materials.

This work demonstrates that capturing structural variability across length scales—through combined small-box and large-box modeling, PDF analysis, and experimental validation—is critical for linking atomic-scale disorder to functional performance. Both

NMC and DRX studies highlight the central role of local distortions, short-range order, and correlated disorder in determining Li transport and thermal stability, providing design principles for next-generation cathode materials.

## LIST OF REFERENCES

[1] Ricci V, Romano P, Stampone N. Estimate of economic impact of EVs Li-ion batteries recovery. *Clean Energy and Sustainability*, 2023, 1, 1005.

[2] Ralls AM, Leong K, Clayton J, Fuelling P, Mercer C, Navarro V, Menezes PL. The role of lithium-ion batteries in the growing trend of electric vehicles. *Materials* (Basel), 2023 Sep 4;16(17):6063.

[3] Tara Energy. (N.d.). *EV Batteries: Understanding Benefits, Challenges, and Operation*. https://taraenergy.com/blog/ev-batteries-understanding-benefits-challenges-and-operation/

[4] USGS, (2025, November 14). *The 2025 List of Critical minerals.* https://www.usgs.gov/news/science-snippet/interior-department-releases-final-2025-list-critical-minerals

[5] Sahin Alacacayir, Irdanto Saputra Lase, Robert Pell, Jordan Lindsay. *Circular Economy Shaping the Future of Lithium-Ion Batteries.* https://www.minviro.com/resources/guides/the-circular-economy-lithium-ion-batteries

[6] Mining Technology, (2024, August 23). *Cobalt production in the Democratic Republic of the Congo and major projects.* https://www.mining-technology.com/data-insights/cobalt-in-the-democratic-republic-of-the-congo/

[7] USGS, (2022, February 22). *U.S. Geological Survey releases 2022 list of critical minerals.* https://www.usgs.gov/news/national-news-release/us-geological-survey-releases-2022-list-critical-minerals

[8] Thackeray, M. M., Kang, S. H., Johnson, C. S., Vaughey, J. T., Benedek, R., Hackney, S. A. Li2MnO3-stabilized LiMO2 (M = Mn, Ni, Co) electrodes for lithium-ion batteries. *J. Mater. Chem*. 2007, 17 (30), 3112−3125.

[9] Chen Y, Huang C. Realizing higher capacity and stability for disordered oxyfluoride cathode materials for Li ion batteries. *RSC Adv.* 2023 Oct 9, 13(42):29343-29353.

[10] Nzereogu, P.U., Omah, A.D., Ezema, F.I., Iwuoha, E.I., Nwanya, A.C. Anode materials for lithium-ion batteries: A review. *Appl. Surf. Sci*. Adv. 2022, 9, 100233.

[11] Hou Zhang, Xudong Gao, Qiuyun Cai, Xiaoyu Zhang, Yinfeng Tian, Min Jia, Wenyong Xie, Yang Du and Xiaohong Yan. Recent progress and perspectives on cation

disordered rock-salt material for advanced Li-ion batteries. *J. Mater. Chem*. A, 2023, 11, 8426-8452.
[12] Whittingham, M. S. Lithium batteries and cathode materials. *Chem. Rev.* (Washington, DC, U. S.) 104, 4271-4302 (2004).
[13] Oak Ridge National Laboratory. (N.d.). *Energy & Energy Storage.* https://neutrons.ornl.gov/industry/energy-energy-storage
[14] Marine Reynaud, Jon Serrano-Sevillano, and Montse Casas-Cabanas. Imperfect battery materials: a closer look at the role of defects in electrochemical performance. *Chem. Mater*. 2023, 35, 3345−3363.
[15] Branford W., Green MA, Neumann DA. Structure and ferromagnetism in Mn (4+) spinels. *Chemistry of Materials*, 2002, 14, p. 1649-1656., DOI 10.1021/cm010857.
[16] Brant, W.R., Schmid, S., Du, G., Brand, H.E.A., Pang, W.K., Peterson, V.K., Guo, Z., Sharma, N. In Situ neutron powder diffraction using custom-made lithium-ion batteries. *J. Vis. Exp*. (93), 52284, doi: 10.3791/52284, 2014.
[17] Mitsubishi Electric. (2023, April 17). *Lithium Nickel Manganese Cobalt Oxide (NMC).* https://www.mitsubishicritical.com/resources/blog/the-runaway-review/lithium-nickel-manganese-cobalt
[18] Thomas E. Ashton, Peter J. Baker, Carlos Sotelo-Vazquez, Charles J. M. Footer, Kenji. M. Kojima, Takeshi Matsukawa, Takashi Kamiyamaf and Jawwad A. Darra. Stoichiometrically driven disorder and local diffusion in NMC cathodes. *J. Mater. Chem*. A, 2021, 9, 10477.
[19] L. Yin, Z. Li, G. S. Mattei, J. Zheng, W. Zhao, F. Omenya, C. Fang, W. Li, J. Li, Q. Xie, E. M. Erickson, J.-G. Zhang, M. S. Whittingham, Y. S. Meng, A. Manthiram and P. G. Khalifah, *Chem. Mater*., 2020, 32, 1002–1010.
[20] Juliette Billaud, Denis Sheptyakov, Sebastien Sallard, Daniela Leanza, Michael Talianker, Judith Grinblat, Hadar Sclar, Doron Aurbach, Petr Novak´ and Claire Villevieille. Li/Fe substitution in Li-rich Ni, Co, Mn oxides for enhanced electrochemical performance as cathode materials. *J. Mater. Chem*. A, 2019, 7, 15215.
[21] Hong Cai, Ruiyong Chen, Mounib Bahri et al. Fluorine-rich oxyfluoride spinel-like $Li_{1.25}Ni_{0.625}Mn_{1.125}O_3F$ utilizing redox-active Ni and Mn for high capacity and improved

cyclability, *ACS Materials Letters* 2023 *5* (2), 527-535, DOI: 10.1021/acsmaterialslett.2c00973.
[22] Thackeray, M. M., Kang, S. H., Johnson, C. S., Vaughey, J. T., Benedek, R.; Hackney, S. A. Li2MnO3-stabilized LiMO2 (M = Mn, Ni, Co) electrodes for lithium-ion batteries. *J. Mater. Chem*. 2007, 17 (30), 3112−3125.
[23] Sébastien Sallard, Juliette Billaud, Denis Sheptyakov, Petr Novák, and Claire Villevieille. Cr-doped Li-rich nickel cobalt manganese oxide as a positive electrode material in Li-ion batteries to enhance cycling stability. *ACS Applied Energy Materials* 2020, 3, 9, 8646-8657.
[24] Xi Zhang, Shun Chen, Jingzhe Zhu, Yizhao Gao. A Critical review of thermal runaway prediction and early-warning methods for lithium-ion batteries. *Energy Mater Adv*. 2023;4:0008.DOI:10.34133/energymatadv.0008.
[25] Kaliaperumal M, Dharanendrakumar MS, Prasanna S, Abhishek KV, Chidambaram RK, Adams S, Zaghib K, Reddy MV. Cause and mitigation of lithium-ion battery failure-A Review. *Materials* (Basel). 2021 Sep 29, 14(19):5676. doi: 10.3390/ma14195676. PMID: 34640071; PMCID: PMC8510069.
[26] Hao Du, Yadong Wang, Yuqiong Kang, Yun Zhao, Yao Tian, Xianshu Wang, Yihong Tan, Zheng Liang, John Wozny, Tao Li, Dongsheng Ren, Li Wang, Xiangming He, Peitao Xiao, Eryang Mao, Naser Tavajohi, Feiyu Kang, and Baohua Li. Side reactions/changes in lithium-ion batteries: Mechanisms and strategies for creating safer and better batteries. *Adv. Mater*. 2024, 36, 2401482.
[27] Linxiao Geng, Jue Liu, David L. Wood, III, Yan Qin, Wenquan Lu, Charl J. Jafta, Yaocai Bai, and Ilias Belharouak. Probing thermal stability of Li-ion battery Ni-rich layered oxide cathodes by means of operando gas analysis and neutron diffraction. *ACS Appl. Energy Mater*. 2020, 3, 7058−7065.
[28] Roland Jung, Philipp Strobl, Filippo Maglia, Christoph Stinner, and Hubert A. Gasteiger. Temperature dependence of oxygen release from LiNi0.6Mn0.2Co0.2O2 (NMC622) cathode materials for Li-ion batteries. *Journal of The Electrochemical Society*, 165 (11) A2869-A2879 (2018).

[29] Y Chu, Y Mu, L. Zou, F. Wu, L Yang, Y Feng, L Zeng. Oxygen release in Ni-rich layered cathode for Li-ion batteries: Mechanisms and mitigation strategies. *ChemElectroChem*, 2024, 11, e202300653 (1 of 21).
[30] Fantai Kong, Chaoping Liang, Luhua Wang, Yongping Zheng, Sahila Perananthan, Roberto C. Longo, John P. Ferraris, Moon Kim, and Kyeongjae Cho. Kinetic stability of bulk LiNiO2 and surface degradation by oxygen evolution in LiNiO2-based cathode materials. *Adv. Energy Mater*. 2018, 1802586.
[31] Yabuuchi, N., Kim, Y. T., Li, H. H., Shao-Horn, Y. *Chem. Mater.* 2008, 20, 4936.
[32] Kim, S. W., Kim, J., Gwon, H., Kang, K. J. *Electrochem. Soc.* 2009, 156, A635.
[33] Kim, J., Park, K. Y., Park, I., Yoo, J. K., Hong, J., Kang, K. *J. Mater. Chem*. 2012, 22, 11964.
[34] Lee, K. K., Yoon, W. S., Kim, K. B., Lee, K. Y., Hong, S. T. *J. Power Sources* 2001, 97−8, 321.
[35] Baba, Y., Okada, S., Yamaki, *J. Solid State Ionics* 2002, 148, 311. 20.
[36] Bang, H. J., Joachin, H., Yang, H., Amine, K., Prakash, *J. J. Electrochem. Soc*. 2006, 153, A731.
[37] MacNeil, D. D., Lu, Z. H., Chen, Z. H., Dahn, J. R. *J. Power Sources* 2002, 108, 8.
[38] Jiang, J., Dahn, J. R. *Electrochem. Commun*. 2004, 6, 39.
[39] Guilmard, M., Croguennec, L., Denux, D., Delmas, *C. Chem. Mater.* 2003, 15, 4476.
[40] Seong-Min Bak, Kyung-Wan Nam, Wonyoung Chang, Xiqian Yu, Enyuan Hu, Sooyeon Hwang, Eric A. Stach, Kwang-Bum Kim, Kyung Yoon Chung, and Xiao-Qing Yang. Correlating structural changes and gas evolution during the thermal decomposition of charged LixNi0.8Co0.15Al0.05O2 cathode materials, *Chem. Mater*. 2013, 25, 337−351, dx.doi.org/10.1021/cm303096e.
[41] Bak, Seong-Min et. al. Structural changes and thermal stability of charged LiNixMnyCozO2 cathode materials studied by combining in situ time-resolved XRD and Mass Spectroscopy, *ACS Applied Materials & Interfaces*, 6, 24, 1944-8244, doi: 10.1021/am506712c, 2014.
[42] Enyuan Hu, Seong-Min Bak, Jue Liu, Xiqian Yu, Yongning Zhou, Steven N. Ehrlich, Xiao-Qing Yang, and Kyung-Wan Nam. Oxygen-release-related thermal

stability and decomposition pathways of LixNi0.5Mn1.5O4 cathode materials. *Chem. Mater.* 2014, 26, 1108−1118, dx.doi.org/10.1021/cm403400y
[43] Y. Chu et al. Oxygen release in Ni-rich layered cathode for LIBs: Mechanisms and mitigating strategies. 2024.
[44] Zhang, Hanlei, Liu, Hao, Piper, Louis F. J., Whittingham, M. Stanley and Zhou, Guangwen. Oxygen loss in layered oxide cathodes for Li-Ion batteries : mechanisms, effects, and mitigation. *Chemical Reviews*, 2022, 122 (6). pp. 5641-5681, https://doi.org/10.1021/acs.chemrev.1c00327, ISSN 0009-2665.
[45] Xiaoyan Xie, Xin Zhang, Xiaokai Ding, Yaowen Wang, Mengmeng Yan, Dong Luo, Guangshe Li, Liping Li. Recent progress on Co-free and Ni-rich layered cathode materials: challenges, improvements and prospect, *Materials Today Energy*, Volume 54, 2025, 102111, ISSN 2468-6069, https://doi.org/10.1016/j.mtener.2025.102111.
[46] P. Reale, D. Privitera, S. Panero, B. Scrosati, *Solid State Ionics* 2007, *178*, 1390.
[47] J. Wandt, A. T. S. Freiberg, A. Ogrodnik, H. A. Gasteiger. Singlet oxygen evolution from layered transition metal oxide cathode materials and its implications for Li-ion batteries, *Mater. Today* 2018, DOI 10.1016/j.mattod.2018.03.037.
[48] C. Wei, Y. Zhang, Y. Zhang, L. Mud, J. Liu, C. Wang, Y. Yang, M. Doeff, P. Pianetta, D. Nordlund, X.-W. Du, Y. Tian, K. Zhao, h J.-S. Lee, F. Lin, Y. Liu. Thermally driven mesoscale chemo mechanical interplay in Li0.5Ni0.6Mn0.2Co0.2O2 cathode materials, *J. Mater. Chem. A* 2018, *6*, 23055.
[49] P. Yan, J. Zheng, M. Gu, J. Xiao, J. G. Zhang, C. M. Wang, *Nat. Commun.* 2017, 8, 1.
[50] J. M. Lim, T. Hwang, D. Kim, M. S. Park, K. Cho, M. Cho, *Sci. Rep.* 2017, 7, 2.
[51] K.W. Nam, S.M. Bak, E. Hu, X. Yu, Y. Zhou, X. Wang, L. Wu, Y. Zhu, K.Y. Chung, X.Q. Yang, *Adv. Funct. Mater.* 2013, *23*, 1047.
[52] S.K.Jung, H.Kim, S. H.Song, S.Lee, J.Kim, K.Kang. Unveiling the role of transition-metal ions in the thermal degradation of layered Ni–Co–Mn cathodes for lithium rechargeable batteries. *Adv. Funct. Mater*. 2022, 32, 108790. https://doi.org/10.1002/adfm.202108790.

[53] Fan Y, Wang X, Bo G, Xu X, See KW, Johannessen B, Pang WK. Operando synchrotron X-Ray Absorption Spectroscopy: A Key tool for cathode material studies in next-generation batteries. *Adv Sci* (Weinh). 2025 Mar;12(10):e2414480. doi: 10.1002/advs.202414480. Epub 2025 Jan 24. PMID: 39853956; PMCID: PMC11905071.
[54] Bassey, Euan N., Reeves, Philip J., Seymour, Ieuan D., Grey, Clare P., 17O NMR spectroscopy in lithium-ion battery cathode materials: Challenges and interpretation, *J. Am. Chem. Soc*., Vol 144, Issue 41, 2022.
[55] Liu X, Xu GL, Yin L, Hwang I, Li Y, Lu L, Xu W, Zhang X, Chen Y, Ren Y, Sun CJ, Chen Z, Ouyang M, Amine K. Probing the thermal-driven structural and chemical degradation of Ni-rich layered cathodes by Co/Mn exchange. *J Am Chem Soc*. 2020 Nov 18;142(46):19745-19753. doi: 10.1021/jacs.0c09961. Epub 2020 Nov 4. PMID: 33147025.
[56] Wang, X., Liu, J., Zhang, J., Wang, Z., Yang, X.Q., Hu, E. Pair Distribution Function analysis of functional materials: Fundamentals and applications in batteries. *Chem. Rev.* 2020, *120* (17), 6509–6553. https://doi.org/10.1021/acs.chemrev.9b00842.
[57] Liu, J., Huq, A., Moorhead-Rosenberg, Z., Manthiram, A., Page, K. Nanoscale Ni/Mn ordering in the high voltage spinel cathode $LiNi_{0.5}Mn_{1.5}O_4$. *Chemistry of Materials* 28, 6817–6821 (2016).
[58] Fagorederbatt. (N.d.). *NMC Series*. https://fagorederbatt.com/product/nmc-series/
[59] Grepow. (2024, June 7). *Rechargeable battery*. https://www.grepow.com/blog/nmc-vs-nca-battery-cell-what-is-the-difference.html
[60] Geldasa FT, Kebede MA, Shura MW, Hone FG. Identifying surface degradation, mechanical failure, and thermal instability phenomena of high energy density Ni-rich NCM cathode materials for lithium-ion batteries: a review. *RSC Adv*. 2022 Feb 16;12(10):5891-5909. doi: 10.1039/d1ra08401a. PMID: 35424548; PMCID: PMC8982025.
[61] Yerkezhan Yerkinbekova, Alisher Kumarov, Batukhan Tatykayev, Almagul Mentbayeva, Eveliina Repo, Ekaterina Laakso. Ni-rich cathode materials with concentration gradients for high-energy and safe lithium-ion batteries: A comprehensive

review. *Journal of Power Sources*, Volume 626, 2025, 235686, ISSN 0378-7753, https://doi.org/10.1016/j.jpowsour.2024.235686.
[62] Hong Cai et al. Fluorine-rich oxyfluoride spinel-like $Li_{1.25}Ni_{0.625}Mn_{1.125}O_3F$ utilizing redox-active Ni and Mn for high capacity and improved cyclability, *ACS Materials Lett.* 2023, 5, 2, 527–535.
[63] NIST. (N.d.). *Scattering table.* https://www.ncnr.nist.gov/resources/n-lengths/elements/li.html
[64] Saaid FI, Kasim MF, Winie T, Elong KA, Azahidi A, Basri ND, Yaakob MK, Mastuli MS, Amira Shaffee SN, Zolkiffly MZ, Mahmood MR. Ni-rich lithium nickel manganese cobalt oxide cathode materials: A review on the synthesis methods and their electrochemical performances. *Heliyon*. 2023 Dec 29;10(1):e23968. doi: 10.1016/j.heliyon.2023.e23968.
[65] Neuefeind, J., Feygenson, M., Carruth, J., Hoffmann, R., & Chipley, K. (2012). The Nanoscale Ordered Materials Diffractometer NOMAD at the Spallation Neutron Source SNS. Nuclear instruments and methods in Physics Research Section B: Beam interactions with materials and atoms, 287, 68–75. https://doi.org/10.1016/j.nimb.2012.04.028.
[66] D. Olds, K. Page, A. Paecklar, P. Peterson, J. Liu, G. Rucker, M. Ruiz-Rodrigues, M. Olsen, M. Pawel, S. Overbury, J. Neilson. A high precision gas flow cell for performing in situ neutron studies of local atomic structure in catalytic materials, 2017.
[67] Geldasa FT, Kebede MA, Shura MW, Hone FG. Identifying surface degradation, mechanical failure, and thermal instability phenomena of high energy density Ni-rich NCM cathode materials for lithium-ion batteries: a review. *RSC Adv*. 2022 Feb 16;12(10):5891-5909. doi: 10.1039/d1ra08401a. PMID: 35424548; PMCID: PMC8982025.
[68] McDonnell TM et al. ADDIE: Advanced Diffraction Environment – a software environment for analyzing neutron diffraction data. *Acta Crystallogr. Sect.* A 73, a377, 2017.
[69] Coehlo A. Topas-Academic V6, Coelho Software 2016.

[70] Larson, A. C., Von Dreele, R. B., General Structural Analysis System (GSAS). Los Alamos National Laboratory Report LAUR 86−748; 2004, Los Alamos National Laboratory: Los Alamos, NM.
[71] National Institute of Standards and Technology. Standard reference material 640e: Line position and line shape standard for powder diffraction (Silicon Powder), Certificate (Gaithersburg, MD: NIST, 2015).
[72] Lobanov N.N, Alte da Veiga, L., *6th European Powder Diffraction Conference* 1998, Abstract P12-16.
[73] Egami T, Billinge S. Underneath the Bragg peaks, structural analysis of complex materials, 7*, Elsevier*, Oxford 2003.
[74] Guilmard, M., Croguennec, L., Denux, D., Delmas, *C. Chem. Mater*. 2003, 15, 4476.
[75] Soroosh Sharifi-Asl, Jun Lu, Khalil Amine, Reza Shahbazian-Yassar. Oxygen release degradation in Li-ion battery cathode materials: Mechanisms and mitigating approaches.
[76] Roujia Chen, Chu Lun Alex Leung, Chun Huang. Exploring the properties of discovered rocksalt battery cathode materials by advanced characterization. *Advan. Functional Materials*, Feb. 2024.
[77] Lee J, Kitchaev DA, Kwon DH, Lee CW, Papp JK, Liu YS, Lun Z, Clément RJ, Shi T, McCloskey BD, Guo J, Balasubramanian M, Ceder G. Reversible $Mn^{2+}/Mn^{4+}$ double redox in lithium-excess cathode materials. *Nature*. 2018 Apr;556(7700):185-190. doi: 10.1038/s41586-018-0015-4. Epub 2018 Apr 11. PMID: 29643482.
[78] O'Quinn et al. Predicting short-range order and correlated phenomena in disordered crystalline materials, *Sci. Adv.* 2020, 6, eabc2758.
[79] B. Ouyang, N. Artrith, Z. Lun, Z. Jadidi, D. A. Kitchaev, H. Ji, A. Urban, G. Ceder, *Adv. Energy Mater*. 2020, 10, 1903240.
[80] J. Ahn, D. Chen, G. Chen, *Adv. Energy Mater*. 2020, 10, 200167.
[81] Chen, Dongchang, Ahn, Juhyeon, Lawrence, Self, Ethan, Nanda, Jagjit. Understanding cation-disordered rocksalt oxyfluoride cathodes, *Journal of Materials Chemistry.*

[82] Huiwen Ji, Alexander Urban, Daniil A. Kitchaev, Deok-Hwang Kwon, Nongnuch Artrith, Colin Ophus, Wenxuan Huang, Zijian Cai, Tan Shi, Jae Chul Kim, Haegyeom Kim & Gerbrand Ceder. Hidden structural and chemical order controls lithium transport in cation-disordered oxides for rechargeable batteries, *NATURE COMMUNICATIONS* (2019) 10:592.
[83] Nathan Szymanski et al. Modeling short-range order in disordered rocksalt Cathodes by Pair Distribution Function analysis. *Chem. Mater*. 2023, 35, 13, 4922–4934.
[84] Sichen Jiao, Yujian Sun, Junyang Wang, Dekai Shi, Yapei Li, Xiangkang Jiang, Fangwei Wang, Yuanpeng Zhang, Jue Liu, Xuelong Wang, Xiqian Yu, Hong Li, Liquan Chen, and Xuejie Huang, The Mechanism of fluorine doping for the enhanced lithium storage behavior in cation-disordered cathode oxide. *Adv. Energy Mater.* 2023, 13, 2301636.
[85] Clement, Lun, Ceder, *Energy Environ. Sci.*, 2020, 13, 345–373.
[86] Kitchaev et al., *Energy Environ. Sci.*, 2018, 11, 2159–2171.
[87] Ouyang et al., *Adv. Energy Mater.*, 2020, 10, 1903240.
[88] Patil, S. *et al.* Alternate synthesis method for high-performance manganese rich cation disordered rocksalt cathodes. *Advanced Energy Materials* 13, 2203207 (2023).
[89] Szymanski, N. J. *et al.* Understanding the fluorination of disordered rocksalt cathodes through rational exploration of synthesis pathways. *Chem. Mater.* 34, 7015–7028 (2022). https://doi.org/10.1021/acs.chemmater.2c01474.
[90] Farrow, C. L. *et al.* PDFfit2 and PDFgui: computer programs for studying nanostructure in crystals. *J. Phys. Condens. Matter* 19, 335219 (2007). https://doi.org/10.1088/0953-8984/19/33/335219.
[91] Tucker, M. G., Keen, D. A., Dove, M. T., Goodwin, A. L. & Hui, Q. RMCProfile: reverse Monte Carlo for polycrystalline materials. *J. Phys. Condens. Matter* **19**, 335218 (2007). https://doi.org/10.1088/0953-8984/19/33/335218.
[92] Kresse, G. & Furthmüller J. Efficient iterative schemes for ab initio total-energy calculations using a plane-wave basis set. *Physical review B* 54, 11169 (1996). https://doi.org/10.1103/physrevb.54.11169.

[93] Chiang, Yet-Ming, Wang, Haifeng, Jang, Young-Il. Electrochemically induced cation disorder and phase transformations in lithium intercalation oxides. *Chem. Mater*., 53, 63, VL 13, 2001, doi: 10.1021/cm000569z https://doi.org/10.1021/cm000569z.
[94] OSTI. (2020, May 3). *Materials Data on Li2TiO3 by Materials Project.* https://www.osti.gov/biblio/1207255.
[95] Tarakina, Nadezda V., et al. Defect crystal structure of new TiO (OH) 2 hydroxide and related lithium salt Li 2 TiO 3. *Dalton Transactions* 39.35 (2010): 8168-8176.
[96] J. P. Perdew, K. Burke, and M. Ernzerhof, *Phys. Rev. Lett*. 77, 3865 (1996). https://doi.org/10.1103/PhysRevLett.77.3865.
[97] J. Sun, A. Ruzsinszky, and J. P. Perdew, *Phys. Rev. Lett.* 115, 036402 (2015). https://doi.org/10.1103/PhysRevLett.115.036402.
[98] A. Zunger, S.H. Wei, L. G. Ferreira, and J. E. Bernard, *Phys. Rev. Lett*. 65, 353–356 (1990). https://doi.org/10.1103/PhysRevLett.65.353.

## VITA

Originally from Moscow, Russia, Margarita Petrova earned her Bachelor's degree in Machine Building from the Moscow Polytechnic University. She later obtained her Master's degree in Materials Science and Engineering from the University of Tennessee, completing a thesis titled "*Cell Contraction, De-adhesion, and Shape Effects by Cohesive Model with Finite Element Simulations*" in 2016. From 2016 to 2020, she worked through Oak Ridge Associated Universities (ORAU) with the Materials Science and Technology Division at Oak Ridge National Laboratory (ORNL). She worked as an instructor in Math and Science Department, Roane State Community College in 2021-2023. In 2023, she returned to the University of Tennessee to join the Energy Science and Engineering Program at the Bredesen Center. Her current research focuses on advancing the understanding of structure–property relationships in cathode materials for lithium-ion batteries using advanced neutron scattering techniques.